Directional Superradiance in a Driven Ultracold Atomic Gas in Free Space

Sanaa Agarwal,[1,2,*] Edwin Chaparro,[1,2] Diego Barberena,[1,2] A. Piñeiro Orioli,[3,4] G. Ferioli,[5] S. Pancaldi,[5] I. Ferrier-Barbut,[5] A. Browaeys,[5] and A.M. Rey[1,2,†]

[1] *Joint Institute for Laboratory Astrophysics (JILA), National Institute of Standards and Technology (NIST), Department of Physics, University of Colorado, Boulder, Colorado 80309, USA*

[2] *Center for Theory of Quantum Matter, University of Colorado, Boulder, Colorado 80309, USA*

[3] *QPerfect, 23 Rue du Loess, 67000 Strasbourg, France*

[4] *University of Strasbourg and CNRS, Centre Européen de Sciences Quantiques (CESQ) and Institut de Science et d'Ingénierie Supramoléculaires (ISIS) (UMR 7006), 67000 Strasbourg, France*

[5] *Institut d'Optique Graduate School, CNRS, Laboratoire Charles Fabry, Universite Paris-Saclay, 91127 Palaiseau, France*

(Received 22 March 2024; revised 16 July 2024; accepted 1 October 2024; published 3 December 2024)

Ultracold atomic systems are among the most promising platforms that have the potential to shed light on the complex behavior of many-body quantum systems. One prominent example is the case of a dense ensemble illuminated by a strong coherent drive while interacting via dipole-dipole interactions. Despite being subjected to intense investigations, this system retains many open questions. A recent experiment carried out in a pencil-shaped geometry [Ferioli *et al.* Nat. Phys. 19, 1345 (2023)] has reported measurements that have seemed consistent with the emergence of strong collective effects in the form of a "superradiant" phase transition in free space, when looking at the light-emission properties in the forward direction. Motivated by the experimental observations, we carry out a systematic theoretical analysis of the steady-state properties of the system as a function of the driving strength and atom number N. We observe signatures of collective effects in the weak-driving regime, which disappear with increasing drive strength as the system evolves into a single-particle-like mixed state comprised of randomly aligned dipoles. Although the steady state features some similarities to the reported superradiant-to-normal nonequilibrium transition, also known as cooperative resonance fluorescence, we observe significant qualitative and quantitative differences, including a different scaling of the critical drive parameter (from N to $\sqrt{N}$). We validate the applicability of a mean-field treatment to capture the steady-state dynamics under currently accessible conditions. Furthermore, we develop a simple theoretical model that explains the scaling properties by accounting for interaction-induced inhomogeneous effects and spontaneous emission, which are intrinsic features of interacting disordered arrays in free space.

DOI: 10.1103/PRXQuantum.5.040335

I. INTRODUCTION

Atoms and photons are among the fundamental building blocks of our universe. Their interactions rule the behavior of our physical world and understanding them is an essential need. However, it is a challenging task, as atom-light interactions can be extremely complex, especially in the context of many-body quantum systems [1,2].

In most relevant situations, a large number of electromagnetic modes remain in the vacuum and the photons just act as passive mediators of excitations between atoms. The net effect is a virtual exchange of excitations that gives rise to dipole-dipole interactions between atoms, with both dispersive and dissipative contributions [3–6]. Despite eliminating the vast number of electromagnetic vacuum modes from the picture and simplifying the complexity to only the atomic degrees of freedom, understanding the consequences of dipolar interactions in dense atomic samples is extremely complicated [7,8] and, apart from special limiting cases [1], it remains a long-standing problem in physical sciences.

For the case of effective two-level atoms, the weak-excitation limit admits a simple semiclassical description and a great deal of theoretical [9,10] and experimental

*Contact author: sanaa.agarwal@colorado.edu
†Contact author: arey@jilau1.colorado.edu

progress has been made in recent years, including the observation of collective level shifts [11–23], line broadening [11,13,17,19–21,24–33], and cooperative subradiant responses [31,34–40] in optically thick [41] and spatially ordered arrays [19,42–46].

Away from the weak-excitation limit, the problem becomes theoretically intractable, at least under current numerical capabilities [47], and many open questions remain. One situation in which important advances have been achieved is the case of ordered arrays, where atoms are initialized in an uncorrelated excited state and allowed to decay collectively without an external drive [48–50]. This case enjoys the simplification that in the thermodynamic limit, ordered arrays can be treated as translationally invariant infinite systems. Although continuous driving adds further complexity, the translational invariance of the problem has enabled better understanding under further assumptions [51–54]. One particularly simple case of the driven-dissipative system is the limit when only permutationally symmetric states, also known as Dicke states [55], are populated. This situation arises naturally in optical cavities, where a single cavity mode talks to all atoms independent of their location in the array. In this limit, the theoretical treatment is significantly simpler and has been a focus of theoretical investigations for decades. One particular case is the so-called cooperative resonance fluorescence (CRF) [56–59] or collective atomic emission [60], which treats the behavior of a group of two-level atoms coupled identically to a single radiation mode. As first proposed by Dicke [55], it leads to a collective decay mechanism, superradiance, which, as has later been theoretically shown, can be stabilized by driving the system below a critical drive strength. In the thermodynamic limit of a large number of atoms (or a large cooperation number), the competition between a coherent drive and decay gives rise to a nonequilibrium second-order phase transition. Below a threshold drive strength, the collective dipole reaches a highly pure steady state characterized by a collective Bloch vector below the equator, pointing at a polar angle at which the superradiant decay and the external drive compensate each other. On the other hand, above a critical drive, the collective dissipation is not enough to stabilize the strongly driven system and at the mean-field (MF) level, the system remains oscillating. Beyond-MF effects dampen the oscillations via phase diffusion and the system becomes a highly mixed state with a distribution centered around the equator.

A recent experiment [61] has reported signatures of the above collective Dicke transition while interrogating a pencil-shaped cloud of N Rb atoms optically excited by a laser propagating along its main axis. The experiment has observed clear manifestations of the two nonequilibrium phases depending on the ratio between the single-atom Rabi frequency, Ω, of the drive and the collective dissipation rate, ΓN_{eff}, characterized by the single-particle decay rate, Γ, and an effective atom number, N_{eff}, which accounts for the finite extent of the diffraction mode of the cloud, $N_{\text{eff}} \propto N$. Above a critical drive $\Omega > \Omega_C$, a scaling of the photon emission rate consistent with N_{eff}^2 has been observed. This scaling has been modified below Ω_C. As the system has crossed the critical point, the characteristics of the superradiant light have changed as well.

Regardless of these clear signatures, as explained in that work [61], the applicability of a fully collective model scaled by an effective atom number to describe the light scattering of an elongated sample in free space is highly unexpected. A justification of its validity starting from a microscopic model remains an open question. In this paper, we solve this issue by performing a detailed study of the light-scattering properties of pencil-shaped disordered arrays of two-level atoms by directly solving a master equation. Our analysis accounts for the spatial extent of the cloud and the dipole-dipole interactions across the array, including spatial fluctuations, elastic dipole-dipole interactions, and single-particle decay. Starting from a mean-field description of the master equation, expected to be valid in the weak- and strong-excitation limits, and complementing it with a moving-average cluster-expansion method (MACEMF) and the cumulant method, we reproduce the experimental observations in all reported parameter regimes. Extended calculations over a larger atom number window reveal a modified scaling, which is not proportional to an effective atom number (N_{eff}) but to the square root of the total number of atoms, ($\sqrt{N}$), in the array.

Our study demonstrates that the observed collective behavior is not valid over a broad parameter regime (see Fig. 1), since it misses important key features of free-space emission, such as single-atom spontaneous emission and the frequency shifts arising from inhomogeneous elastic dipolar interactions. By combining the latter mechanisms with collective decay plus drive, we are able

CRF model: $\Omega_C^{\text{CRF}} = \Gamma N/2$		Dipolar model: $\Omega_C^{\text{dipolar}} \propto \Gamma\sqrt{N}$	
$\Omega \ll \Omega_C^{\text{CRF}}$	$\Omega \gg \Omega_C^{\text{CRF}}$	$\Omega \ll \Omega_C^{\text{dipolar}}$	$\Omega \gg \Omega_C^{\text{dipolar}}$
$\langle \hat{S}_z \rangle \neq 0$	$\langle \hat{S}_z \rangle = 0$	$\langle \hat{S}_z \rangle \neq 0$	$\langle \hat{S}_z \rangle = 0$
$\langle \hat{S}_+ \hat{S}_- \rangle \propto N^2$	$\langle \hat{S}_+ \hat{S}_- \rangle \propto N^2$	$\langle \tilde{\hat{S}}_+ \tilde{\hat{S}}_- \rangle \propto N^{1<\alpha<2}$	$\langle \tilde{\hat{S}}_+ \tilde{\hat{S}}_- \rangle \to N/2$
$\langle \hat{S}_x \rangle = 0$	$\langle \hat{S}_x \rangle = 0$	$\langle \tilde{\hat{S}}_x \rangle \neq 0$	$\langle \tilde{\hat{S}}_x \rangle \to 0$
$g_2(0) = 1$	$g_2(0) \sim 1.2$	$\tilde{g}_2(0) \sim 1$	$\tilde{g}_2(0) \to 2$

FIG. 1. A summary of the important steady-state observables in the weak—($\Omega \ll \Omega_C$) and strong—($\Omega \gg \Omega_C$) driving regimes in the CRF (left) and dipolar (right) models, with respect to a "critical" drive Ω_C for each model. For the CRF model, we have the atomic inversion, $\langle \hat{S}_z \rangle$, as the order parameter of the regimes, the intensity, $\langle \hat{S}_+ \hat{S}_- \rangle$, the nondriven part of the atomic coherence, $\langle \hat{S}_x \rangle$, and the total equal-time two-photon correlation function, $g_2(0)$. For the dipolar model, the corresponding observables are in the spiral basis [defined in Eq. (4)].

to qualitatively reproduce all the features observed in the mean-field calculations that account for microscopic details. In the future, it will be interesting to push experiments to more dense regimes where the mean-field model becomes invalid and a genuine quantum treatment would be required in order to properly capture the role of photon-mediated dipolar interactions in driven ultracold atoms.

In the spirit of quantum simulation, our analysis takes advantage of state-of-the-art experimental capabilities in regimes challenging for theory, uses them to develop new theoretical insights that shed light on long-standing problems, and makes predictions to further inspire experimental work.

In Sec. II, we introduce the dipolar model, which describes our system at the microscopic level. We further discuss the extremely dilute and dense limiting cases, which are analytically solvable and useful for understanding the role of interactions in different driving regimes. In Sec. III, we study the steady state of the dipolar model using mean-field numerics in the weak- and strong-driving regimes, and we compare its emergent properties with the CRF and noninteracting models. Using these insights, we propose a phenomenological model in Sec. IV, which accounts for the inhomogeneity of dipolar interactions, is analytically tractable at the mean-field level, and qualitatively reproduces the dipolar model. In Sec. V, we compare our steady-state and dynamics results with the experimental data [61], and find fair agreement for most observables. Lastly, in Sec. VI, we discuss some concluding remarks and future directions.

II. QUASI-ONE-DIMENSIONAL GAS OF DIPOLAR-INTERACTING ATOMS

A. Dipolar model

We consider a three-dimensional elongated (pencil-shaped) gas of N pointlike atoms fixed at their Gaussian-sampled positions $\{\vec{r}_k\}$, as shown in Fig. 2. The atoms have linewidth (single-atom decay rate) Γ and are driven by a coherent laser drive with Rabi strength $\Omega = |\vec{E}\cdot\vec{d}|/\hbar$ (where $\vec{E}$ is the electric field amplitude of the laser and $\vec{d}$ is the transition dipole moment of the atom), detuning $\Delta = \omega_L - \omega_0$ from the atomic transition (frequency ω_0), wave vector $\vec{k}_L$, and polarization $\hat{e}_L$. The quantization axis $\hat{e}_0$ is along the $\hat{z}$ axis and the axial direction of the gas is along the $\hat{x}$ axis. As in Ref. [61], we consider the case in which $\hat{e}_L = \hat{e}_y = \hat{y}$, i.e., the driving laser is linearly polarized and excites the σ_+-transition between the hyperfine levels $|F=2, m_F=2\rangle \leftrightarrow |F=3, m_F=3\rangle$. The atoms interact via induced dipole-dipole interactions mediated by the vacuum electromagnetic modes [1].

We assume that the atomic cloud is cold enough that we can neglect motion of the atoms, treat them as frozen during the dynamics, and only focus on the internal-state

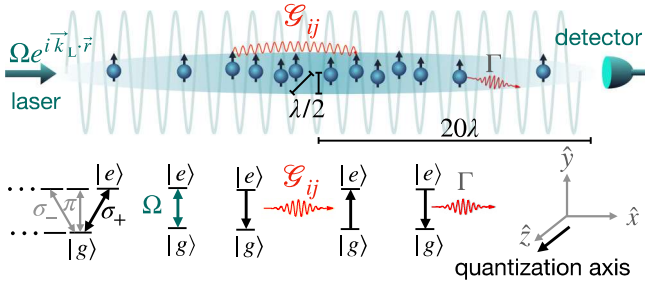

FIG. 2. A schematic of a pencil-shaped ultracold gas of frozen two-level atoms interacting via photon-mediated interactions, with elastic ($\mathrm{Re}\,\mathcal{G}_{ij}$) and inelastic ($\mathrm{Im}\,\mathcal{G}_{ij}$) components. A continuous laser drive excites the atoms on resonance with Rabi frequency Ω, wave vector $\vec{k}_L = 2\pi/\lambda\hat{x}$, and polarization $\hat{e}_L = \hat{y}$ (perpendicular to the quantization axis, $\hat{z}$). Atoms spontaneously emit photons into free space at rate Γ.

dynamics spanned by the two relevant levels in each atom ($|g\rangle \equiv |F=2, m_F=2\rangle$ ground and $|e\rangle \equiv |F=3, m_F=3\rangle$ excited), which define a spin-1/2 system. Under these conditions, which are similar to the system realized in Ref. [61], the state of an atom can be described by spin-1/2 Pauli operators: $\hat{\sigma}_k^z = |e_k\rangle\langle e_k| - |g_k\rangle\langle g_k|$, $\hat{\sigma}_k^+ = |e_k\rangle\langle g_k|$, and $\hat{\sigma}_k^- = |g_k\rangle\langle e_k|$, for an atom k. The collective spin operators are denoted as $\hat{S}_\alpha = \sum_{k=1}^N \hat{\sigma}_k^\alpha/2$ for $\alpha \in \{x,y,z\}$ and $\hat{S}_\pm = \sum_{k=1}^N \hat{\sigma}_k^\pm$.

The dynamics of the system are governed by the master equation obtained upon adiabatically eliminating the photonic degrees of freedom, $\dot{\hat{\rho}} = -i[\hat{H}, \hat{\rho}] + \mathcal{L}(\hat{\rho})$, where $\hat{H}$ is the Hamiltonian, which leads to unitary evolution, and $\mathcal{L}(\hat{\rho})$ is the Lindbladian superoperator, which accounts for all the dissipative processes. The Hamiltonian for the system is given as $\hat{H} = \hat{H}_0 + \hat{H}_{\mathrm{int}}$, where (setting $\hbar = 1$)

$$\hat{H}_0 = -\frac{\Omega}{2}\sum_k (e^{i(\vec{k}_L\cdot\vec{r}_k - \pi/2)}\hat{\sigma}_k^+ + \mathrm{h.c.}) - \Delta\hat{S}_z \tag{1}$$

is the single-particle laser drive and

$$\hat{H}_{\mathrm{int}} = -\sum_{j\neq k}\mathcal{R}_{kj}\hat{\sigma}_k^+\hat{\sigma}_j^- \tag{2}$$

accounts for the dipole-dipole interaction. It sums over pairwise exchange processes among two different atoms in the array, with the interaction strength given by the free-space electromagnetic Green's tensor

$$G(\mathbf{r}) = \left(\frac{3\Gamma}{4}\right)\left\{(1-\hat{r}\otimes\hat{r})\left(\frac{e^{ik_0 r}}{k_0 r}\right) + (1-3\hat{r}\otimes\hat{r})\left[\left(\frac{ie^{ik_0 r}}{(k_0 r)^2}\right) - \left(\frac{e^{ik_0 r}}{(k_0 r)^3}\right)\right]\right\},$$

where $\mathbf{r}$ is the vector connecting the two interacting atoms and $k_0 = 2\pi/\lambda$ (λ is the atomic transition wavelength).

The elastic part is determined by the real part of $G(\mathbf{r})$, $\mathcal{R}_{kj} = \hat{e}_+^{*\mathrm{T}} \cdot \mathrm{Re}\,[G(\vec{r}_{kj})] \cdot \hat{e}_+$, where T implies transpose. Self-interactions are set to zero: $\mathcal{R}_{kk} = 0$. The Lindbladian for the system is expressed as

$$\mathcal{L}(\hat{\rho}) = \sum_{j,k} \mathcal{I}_{kj} \left(2\hat{\sigma}_j^- \hat{\rho} \hat{\sigma}_k^+ - \{\hat{\sigma}_k^+ \hat{\sigma}_j^-, \hat{\rho}\} \right), \tag{3}$$

where $\mathcal{I}_{kj} = \hat{e}_+^{*\mathrm{T}} \cdot \mathrm{Im}\,[G(\vec{r}_{kj})] \cdot \hat{e}_+$ is the inelastic dipolar-interaction coefficient and $\mathcal{I}_{kk} = \Gamma/2$ is the spontaneous-emission decay rate. We define the total dipolar-interaction coefficient as $\mathcal{G}_{kj} = \mathcal{R}_{kj} + i\mathcal{I}_{kj}$.

For simplicity, we define a "spiral" basis, in which we absorb the drive phase in the coherences, as

$$\hat{\tilde{\sigma}}_j^{\pm} = \hat{\sigma}_j^{\pm} e^{\pm i(\vec{k}_\mathrm{L} \cdot \vec{r}_j - \pi/2)}. \tag{4}$$

Then, the spiral collective spin operators are $\hat{\tilde{S}}_\pm = \sum_{j=1}^N \hat{\sigma}_j^{\pm} e^{\pm i(\vec{k}_\mathrm{L} \cdot \vec{r}_j - \pi/2)}$, $\hat{\tilde{S}}_x = (\hat{\tilde{S}}_+ + \hat{\tilde{S}}_-)/2$, $\hat{\tilde{S}}_y = -i(\hat{\tilde{S}}_+ - \hat{\tilde{S}}_-)/2$, and $\hat{\tilde{S}}_z = \hat{S}_z$. Accordingly, we also define new interaction coefficients $\tilde{\mathcal{G}}_{kj} = \mathcal{G}_{kj} e^{-i\vec{k}_\mathrm{L} \cdot \vec{r}_{kj}}$, $\tilde{\mathcal{R}}_{kj} = \mathcal{R}_{kj} e^{-i\vec{k}_\mathrm{L} \cdot \vec{r}_{kj}}$, and $\tilde{\mathcal{I}}_{kj} = \mathcal{I}_{kj} e^{-i\vec{k}_\mathrm{L} \cdot \vec{r}_{kj}}$. In the spiral basis, the Hamiltonian and the Lindbladian are given as

$$\hat{H}_0 = -\Omega \hat{\tilde{S}}_x - \Delta \hat{S}_z, \tag{5}$$

$$\hat{H}_{\mathrm{int}} = -\sum_{j \neq k} \tilde{\mathcal{R}}_{kj} \hat{\tilde{\sigma}}_k^+ \hat{\tilde{\sigma}}_j^-, \tag{6}$$

$$\mathcal{L}(\hat{\rho}) = \sum_{j,k} \tilde{\mathcal{I}}_{kj} \left(2\hat{\tilde{\sigma}}_j^- \hat{\rho} \hat{\tilde{\sigma}}_k^+ - \{\hat{\tilde{\sigma}}_k^+ \hat{\tilde{\sigma}}_j^-, \hat{\rho}\} \right). \tag{7}$$

Thus, the drive acts collectively along the spiral-$\hat{x}$ direction in the Bloch sphere. Hereafter, we will work in the spiral basis and also set $\Delta = 0$, unless otherwise mentioned.

Similar to the experimental protocol in Ref. [61], we initialize all the atoms in the ground state $|g\rangle^{\otimes N}$ and continuously drive them on resonance with the atomic transition, i.e., $\Delta = 0$. The excitation of atoms by the drive is counteracted by the free-space single-particle and collective emission, which generates damping, allowing the system to eventually reach its steady state. To characterize the system across a wide range of drive strengths, Ω, we look at the collective spin observables in the steady state, namely, the atomic inversion $\langle \hat{S}_z \rangle$, the absolute value of the spiral atomic coherence $|\langle \hat{\tilde{S}}_+ \rangle|$, and its real part $|\langle \hat{\tilde{S}}_x \rangle|$.

The intensity operator describing the photon emission from the atomic sample along a direction $\vec{k}$ can be written in terms of the spin operators as [4,62,63],

$$\hat{\mathcal{I}}(\vec{k}) \equiv I_0(\vec{k}) \sum_{i,j} \hat{\sigma}_i^+ \hat{\sigma}_j^- e^{i\vec{k} \cdot (\vec{r}_i - \vec{r}_j)}, \tag{8}$$

where $I_0(\vec{k})$ is a proportionality factor that accounts for the geometry of the dipolar emission pattern. In the spiral basis, the expectation value of the intensity can be expressed as $I(\vec{k}) \equiv \langle \hat{\mathcal{I}}(\vec{k}) \rangle \equiv I_0(\vec{k}) \sum_{i,j} \langle \hat{\tilde{\sigma}}_i^+ \hat{\tilde{\sigma}}_j^- \rangle e^{i(\vec{k} - \vec{k}_\mathrm{L}) \cdot (\vec{r}_i - \vec{r}_j)}$. The intensity along the forward direction, $\vec{k} = \vec{k}_\mathrm{L}$, features very interesting properties and will be the focus of this study. This direction is special because it is the direction along which the driving laser imposes coherence and, therefore, the intensity can be enhanced due to constructive interference.

We also look into the equal-time two-photon correlation function, defined as [63]

$$\tilde{g}_2(\vec{k}, \vec{k}') = \frac{\langle : \hat{\mathcal{I}}(\vec{k}) \hat{\mathcal{I}}(\vec{k}') : \rangle}{I(\vec{k}) I(\vec{k}')}, \tag{9}$$

which gives the likelihood of simultaneously emitting a photon along $\vec{k}'$ and another photon along the $\vec{k}$ direction. The "::" in the above expression implies that it needs to be evaluated using normal-ordered operators. In the experiment [61] in question, the detector was placed in the forward direction to measure the above-mentioned observables. Even though the experiment did not measure the atomic coherence, we will include it in our study as it is useful for gaining an intuitive understanding of the system. In addition to the steady state, we also compute the dynamics of the forward intensity, $I(\vec{k}_\mathrm{L}, t)$, and the excitation fraction,

$$n_e(t) = \frac{1}{2N} \sum_{j=1}^N \left(\langle \hat{\sigma}_j^z(t) \rangle + 1 \right). \tag{10}$$

In the following, we use these observables to investigate distinct key features of the system as a function of the strength of the drive, from the weak- to the strong-driving regimes. To understand the role of interactions, we consider the cases of the extremely dense and dilute limits, which are analytically tractable and well studied. Then, we study the moderately dense ensemble of the experiment (Fig. 2) and compare it with the extremely dilute and dense limits as a means of investigating the behaviors emergent from dipolar interactions. Similar to the experiment, we keep the size of the atomic cloud fixed at an rms axial length $l_{\mathrm{ax}} = 20\lambda$ and radial length $l_{\mathrm{rad}} = \lambda/2$, as shown in Fig. 2. By varying N, we can tune the density of the cloud and, thereby, the strength of the dipole-dipole interactions between the atoms.

B. Cooperative resonance fluorescence (CRF)

In the limit in which all the atoms are confined within a single wavelength, $|r_{0,N}| < \lambda$, we have $\mathcal{R}_{kj} \sim 1/(|r_{kj}|/\lambda)^3, \mathcal{I}_{kj} \to \Gamma/2$. If we choose to neglect the elastic part of the interactions ($\mathcal{R}_{kj} = 0$) and freeze the motion of the atoms, we can emulate the situation found in an optical cavity, where all the atoms interact via a single

electromagnetic mode. When the cavity mode is set on resonance with the atomic transition, the elastic interactions are suppressed and the dominant interactions are the ones responsible for collective decay or superradiance, via which atoms emit collectively at an enhanced emission rate ΓN. In the presence of an additional drive, Ω, the system reduces to the well-studied CRF model, which describes a system of N atoms driven with a resonant laser drive at a Rabi frequency Ω and subject to collective decay (superradiance) described by the jump operator $\sqrt{\Gamma}\hat{S}_-$ with $\hat{S}_\pm = \sum_i \hat{\sigma}_i^\pm$ [64]. Here, we use the notation CRF to distinguish from the so-called Dicke model [65–67], which contains both the rotating and counter-rotating terms. In the CRF model, the counter-rotating terms are irrelevant and are therefore neglected. The master equation governing the dynamics of the CRF model is given by

$$\partial_t \hat{\rho} = -i\Omega\left[\hat{S}_x, \hat{\rho}\right] + \frac{\Gamma}{2}\left(2\hat{S}_-\hat{\rho}\hat{S}_+ - \left\{\hat{S}_+\hat{S}_-, \hat{\rho}\right\}\right), \quad (11)$$

where the drive, Ω, is applied along the x direction of the Bloch sphere. This model has been widely studied and many of the results presented here are well known [68–70]. However, for completeness, we review the main features of this model and use them to later compare with the microscopic model.

The CRF exhibits a steady-state phase transition at a critical frequency $\Omega_C^{\mathrm{CRF}} = N\Gamma/2$ [71], which delineates two distinct steady-state behaviors depending on the dimensionless parameter $\beta = \Omega/\Omega_C^{\mathrm{CRF}}$. For $\beta < 1$, the system is in the "superradiant phase," where the drive is balanced by the collective emission, canceling the total electric field experienced by the collective dipole. We use quotation marks to remark that this regime was initially referred to instead as "superfluorescent" by the authors [56,58,71]. In this phase, the collective dipole lies in the y-z plane of the Bloch sphere at an angle θ from the south pole, given by $\sin\theta = \beta$. For $\beta > 1$, the system transitions into a highly mixed steady state, known as the "normal" phase. The statistical mixture arises from the collective emission not being strong enough to compensate the excitation from the drive. As the atomic self-radiated field is not canceled by the drive, the dipoles undergo collective Rabi flopping. Although Rabi oscillations persist at long times at the mean-field level, quantum fluctuations lead to phase diffusion, which dampens the oscillations and destroys the coherences, although the system always remains in the collective manifold by construction. These two distinct steady-state behaviors are separated by a second-order phase transition at $\beta = 1$, as shown in Fig. 3(a).

Here, it is important to note that Ref. [61] has used the opposite convention and denoted the $\beta > 1$ regime as the superradiant phase. This is inspired by Refs. [69,72] and

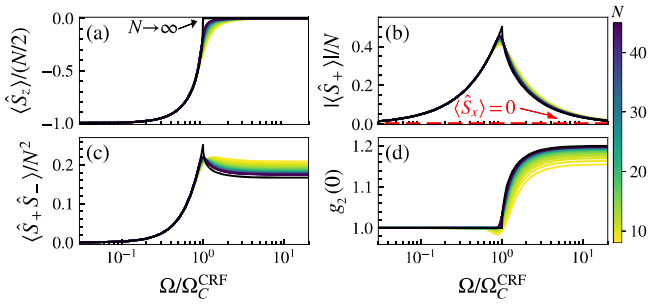

FIG. 3. The steady state of the CRF model using exact diagonalization (extremely dense limit, $r_{ij} \to 0$, and artificially setting $\mathcal{R}_{ij} = 0$). (a) The atomic inversion, $\langle\hat{S}_z\rangle/(N/2)$, shows the superradiant phase transition in the thermodynamic limit. (b) The total coherence, $|\langle\hat{S}_+\rangle|/N = |\langle\hat{S}_y\rangle|/N$, is driven by the laser drive, which is along the $\hat{S}_x$ direction, such that $\langle\hat{S}_x\rangle = 0$. (c) The intensity scales as N^2 and remains constant as Ω is varied in the strong-driving regime (due to preservation of $\langle\hat{\mathbf{S}}^2\rangle = \langle\hat{S}_+\hat{S}_-\rangle + \langle\hat{S}_z^2\rangle = N(N+1)/4$). (d) The two-photon correlation function $g_2(0)$ does not reach the maximally mixed state ($g_2(0) = 2$) due to preserved quantum correlations. The $N \to \infty$ curves correspond to Eqs. (12)–(16).

the fact that Eq. (11) has a discrete symmetry characterized by its invariance under a mirror reflection $\hat{S}_x \to -\hat{S}_x$, followed by complex conjugation. This mirror symmetry of the Lindblad generator is spontaneously broken in the $\beta > 1$ phase and therefore, under this view, this is the phase featuring spontaneous symmetry breaking. For the purpose of this work, this is just a different convention and does not affect our conclusions. We will stick to the more standard CRF convention that uses $\hat{S}_z$ as the physically motivated order parameter and denotes the $\beta < 1$ regime as the superradiant phase.

By doing a Holstein-Primakoff expansion around the mean-field steady state in the superradiant regime as well as introducing a semiclassical method to average in the normal phase, we can express the steady state in the thermodynamic limit ($N \to \infty$) analytically across all driving regimes by varying β (with $\eta = \sqrt{\beta^2 - 1}$) as (for a derivation, see Appendix C)

$$\langle\hat{S}_z\rangle = \begin{cases} -\frac{N}{2}\sqrt{1-\beta^2}, & \beta < 1, \\ 0, & \beta \geq 1, \end{cases} \quad (12)$$

$$\langle\hat{S}_x\rangle = 0, \quad (13)$$

$$\langle\hat{S}_y\rangle = \begin{cases} \frac{N}{2}\beta, & \beta < 1, \\ \frac{N}{2}\left(\beta - \frac{\eta}{\beta\arctan\left(\frac{1}{\eta}\right)}\right), & \beta \geq 1, \end{cases} \quad (14)$$

$$\langle \hat{S}_+ \hat{S}_- \rangle = \begin{cases} \frac{N^2}{4}\beta^2, & \beta < 1, \\ \frac{N^2}{4}\left(\beta^2 - \frac{\eta}{\arctan\left(\frac{1}{\eta}\right)}\right), & \beta \geq 1, \end{cases} \tag{15}$$

$$g_2(0) = \begin{cases} 1, & \beta < 1, \\ \eta\left(\frac{\beta^4}{\eta}\arctan\left(\frac{1}{\eta}\right) - \beta^2 - \frac{2}{3}\right) \\ \times \arctan\left(\frac{1}{\eta}\right)\left(\beta^2 \arctan\left(\frac{1}{\eta}\right) - \eta\right)^2, & \beta \geq 1. \end{cases} \tag{16}$$

$g_2(0)$ is a short-hand for setting both $\vec{k}$ and $\vec{k}'$ to 0 in $g_2(\vec{k}, \vec{k}')$, defined earlier in Eq. (9). For this phase transition, the order parameter is the population inversion, $\langle \hat{S}_z \rangle$, which is nonzero in the superradiant phase and zero in the normal phase [Eq. (12)]. $\langle \hat{S}_z \rangle$ is continuous but features an abrupt change in its derivative at the critical point in the thermodynamic limit ($N \to \infty$), as shown in Fig. 3(a). The finite-N steady state in Fig. 3 is obtained using exact diagonalization.

The observable $\langle \hat{S}_x \rangle$ is conserved and is zero in all regimes [Eq. (13)]. This is a distinguishing feature of this model, which will become important when comparing with the other models in this paper. Thus, the atomic coherence is purely imaginary, $\langle \hat{S}_+ \rangle = i\langle \hat{S}_y \rangle$. In the superradiant phase, $\langle \hat{S}_y \rangle$ grows linearly with β. On the other hand, as β is increased in the normal phase, the steady state becomes more and more mixed and $\langle \hat{S}_y \rangle$ goes to zero, as shown in Fig. 3(b).

The photon emission rate (intensity), $I = \langle \hat{S}_+ \hat{S}_- \rangle$, at a fixed β, increases as $N^2\beta^2$ in the superradiant phase. In the normal phase, the intensity still scales as N^2, reflecting the collective nature of the system, as $\langle \hat{\mathbf{S}} \cdot \hat{\mathbf{S}} \rangle = N/2(N/2 + 1)$, where $\hat{\mathbf{S}} = \{\hat{S}_x, \hat{S}_y, \hat{S}_z\}$. However, the normal phase intensity is independent of β due to the mixed nature of the state in the normal phase. In fact, for $\beta \gg 1$, the intensity reaches the asymptotic value of $I = N^2/6$, as shown in Fig. 3(c). The coherent nature of the steady state in the superradiant phase is also evident in the value of the two-photon correlation function [Fig. 3(d)], as $g_2(0) = 1$ for $\beta < 1$, in the large-N limit. In the normal phase, on the contrary, the system enters a regime in which $g_2(0) > 1$, suggesting the mixed nature of the steady state and the build-up of classical correlations.

C. Noninteracting model

In the extremely dilute limit, the mean inter-atomic distance is large, $|\bar{r}_{ij}| \gg \lambda$, and thus to a good approximation we can neglect the interactions in Eqs. (6) and (7) by setting $\mathcal{R}_{kj} = 0$ and $\mathcal{I}_{k\neq j} = 0$. This gives a simplified master equation for the noninteracting model, $\dot{\hat{\rho}} = -i[\hat{H}_0, \hat{\rho}] + \mathcal{L}_0(\hat{\rho})$, that describes an array of independent atoms coherently interacting with a classical laser drive while spontaneously emitting photons at a rate Γ. The Lindbladian, $\mathcal{L}_0(\hat{\rho}) = (\Gamma/2)\sum_j \left(2\hat{\tilde{\sigma}}_j^- \hat{\rho} \hat{\tilde{\sigma}}_j^+ - \{\hat{\sigma}_j^z, \hat{\rho}\}/2 - \hat{\rho}\right)$, captures the single-particle spontaneous emission. The laser drive acts as an effective global magnetic field, $\vec{B}_L = \{\Omega/2, 0, \Delta/2\}$. The single-atom density matrix and, thus, the spin observables are identical for all atoms in this noninteracting limit, i.e., $\langle \vec{\hat{\tilde{\sigma}}} \rangle = \{\langle \hat{\tilde{\sigma}}^x \rangle, \langle \hat{\tilde{\sigma}}^y \rangle, \langle \hat{\tilde{\sigma}}^z \rangle\}$, and their dynamics can be described by the well-known Bloch equations as

$$\frac{d\langle \vec{\hat{\tilde{\sigma}}} \rangle}{dt} = 2\langle \vec{\hat{\tilde{\sigma}}} \rangle \times \vec{B}_L - \vec{f}\,(\langle \vec{\hat{\tilde{\sigma}}} \rangle), \tag{17}$$

where $\vec{f}\,(\langle \vec{\hat{\tilde{\sigma}}} \rangle) = -(\Gamma/2)[\langle \vec{\hat{\tilde{\sigma}}} \rangle + (\langle \hat{\tilde{\sigma}}^z \rangle + 2)\hat{z}]$ accounts for the damping. Note that the results of this system are well known and easy to obtain analytically. Here, we discuss the particular case in which the laser wave vector is aligned to the observation direction, a condition in which phase matching can be achieved.

For the on-resonant case ($\Delta = 0$), the steady-state Bloch vector is obtained as

$$\langle \hat{\tilde{\sigma}}^+ \rangle = i\frac{\Omega}{\Gamma}\langle \hat{\sigma}^z \rangle, \quad \langle \hat{\sigma}^z \rangle = -R \equiv -\frac{1}{1 + 2(\Omega/\Gamma)^2} \tag{18}$$

and the steady-state intensity is

$$I(\vec{k}) = I_0(\vec{k})\frac{(\Omega/\Gamma)^2}{1 + 2(\Omega/\Gamma)^2}\left[N + \sum_{j,i\neq j}\frac{e^{i(\vec{k}-\vec{k}_L)\cdot(\vec{r}_i - \vec{r}_j)}}{1 + 2(\Omega/\Gamma)^2}\right], \tag{19}$$

which is dominated by the coherences in the weak-driving regime ($\Omega \ll \Gamma$) and by the incoherent single-particle-like term in the strong-driving regime ($\Omega \gg \Gamma$). In the large-N limit, the steady-state intensity can be obtained analytically by converting the above sum to an integral (with $\hat{k} = \{\cos\theta, \sin\theta\cos\phi, \sin\theta\sin\phi\}$), as

$$I(\hat{k}) \propto \frac{2\left(\frac{\Omega}{\Gamma}\right)^4 N}{\left[1 + 2\left(\frac{\Omega}{\Gamma}\right)^2\right]^2}\left[1 + \frac{Ne^{-4\pi^2\left(\sigma_{ax}^2(1-\cos\theta)^2 + \sigma_{rad}^2\sin^2\theta\right)}}{2(\Omega/\Gamma)^2}\right], \tag{20}$$

where σ_{ax} and σ_{rad} are the axial and radial extents of the cloud, respectively. As discussed earlier, when the laser wave vector aligns with the direction of observation ($\vec{k} = \vec{k}_L \Rightarrow \theta = 0$), the imprinted phases interfere constructively. In the weak-driving limit, the forward emission is dominated by its coherent part, $I(\vec{k}_L) \approx$

$I_0(\vec{k}_L)|\langle\hat{\tilde{\sigma}}^+\rangle|^2 N(N-1)$. This N^2 enhancement of the emission rate is only seen in the forward direction and vanishes exponentially fast with increasing θ when $\theta \ll 1$ [Eq. (A20)]. Along other $\vec{k}$, the phases in Eq. (19) do not cancel and the intensity, dominated by its incoherent part, scales as N far away from $\vec{k}_L$. It is worth noting that this N^2 enhancement is not due to quantum correlations and arises trivially from the coherences of the atoms [17,73,74].

For comparison with the other models in this work, we define the notion of a "critical" drive strength, $\Omega_C^{\text{nonint.}}$, that maximizes the "forward" intensity. There is, however, no phase transition in the noninteracting model. This definition of the critical drive is inspired by the CRF model, in which the total coherence and the total intensity peak at the critical drive strength and a phase transition is observed (for details, see Sec. II B). For the noninteracting model, we set $d\langle\hat{\tilde{\sigma}}^+\rangle/d\Omega = 0$ to obtain the critical drive strength as $\Omega_C^{\text{nonint.}} = \Gamma/\sqrt{2}$.

As shown in Fig. 4(a), in the weak-driving limit ($\Omega \ll \Omega_C^{\text{nonint.}}$), the forward intensity scales as $I(\vec{k}_L) \propto (N\Omega/\Gamma)^2$, as shown in Fig. 4(c). Moreover, we find that $\tilde{g}_2(0) = 1$ [Eq. (A11)] in this limit, as shown in Fig. 4(d), which reflects the fact that the system is in a coherent state, with the majority of the atoms in the ground state. $\tilde{g}_2(0)$ is a short-hand for setting both $\vec{k}$ and $\vec{k}'$ to $\vec{k}_L$ in $g_2(\vec{k},\vec{k}')$, defined earlier in Eq. (9).

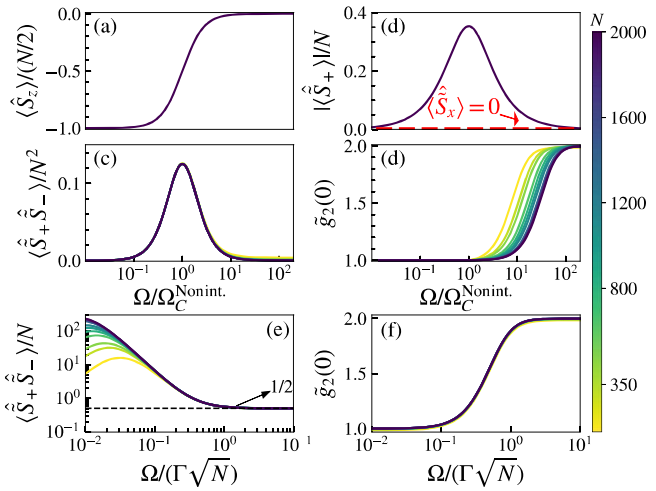

FIG. 4. The steady state in the noninteracting (dilute) limit across driving regimes. (a) The atomic inversion, $\langle\hat{S}_z\rangle/(N/2)$. (b) The total coherence, $|\langle\hat{\tilde{S}}_+\rangle|/N = |\langle\hat{\tilde{S}}_y\rangle|/N$, is driven by the laser in the $\hat{\tilde{S}}_x$ direction such that $\langle\hat{\tilde{S}}_x\rangle = 0$. (c),(e) The "forward" intensity (along the axial direction) scales as (c) N^2 in the weak-driving regime and as (e) N in the strong-driving regime ($\langle\hat{S}_z\rangle/(N/2) \to 0$). (d) The two-photon correlation function $\tilde{g}_2(0)$ in the "forward" direction. (e),(f) Due to the constructive interference of coherences in the "forward" direction, an N-dependent stronger drive ($\Omega \gtrsim \Gamma\sqrt{N}$) is needed to reach the thermal state ($\langle\hat{\tilde{S}}_+\hat{\tilde{S}}_-\rangle \to N/2$, $\tilde{g}_2(0) \to 2$).

In the strong-driving limit ($\Omega \gg \Omega_C^{\text{nonint.}}$), radiative decay disrupts the coherences and leads to a completely mixed steady state [$R \to 0$ in Eq. (18)]. In this mixed state, the Bloch vector of each spin-1/2 (atomic dipole) is reduced to a point at the center of the Bloch sphere such that $\langle\hat{\sigma}^z\rangle \to 0$ [Fig. 4(a)] and $|\langle\hat{\tilde{\sigma}}^+\rangle| \to 0$ [Fig. 4(b)]. In the absence of a finite coherence, there is no constructive interference in the forward direction, i.e., $I(\vec{k}_L) \propto N/2$ [Fig. 4(e)]. We obtain $\tilde{g}_2(0) = 2$ in this limit, as shown in Fig. 4(d), since the system is in a thermal state. As shown in Fig. 4(f), a very strong drive, $\Omega \gtrsim \Gamma\sqrt{N}$, is needed to fully reach this condition. This N-dependent drive scaling emerges due to the N^2 enhancement from the constructive interference of coherences and is further explained in Appendix A.

Lastly, the on-resonant drive Hamiltonian commutes with $\hat{\tilde{\sigma}}^x$, so starting from $\langle\hat{\tilde{\sigma}}^x\rangle = 0$ in the initial state, it remains zero at all times, irrespective of Ω, as shown in Fig. 4(b).

III. MEAN-FIELD DIPOLAR MODEL

A. General description

For a general distribution of atomic positions, the interacting system is free to explore an exponentially large Hilbert space (2^N) and its exact dynamics are not tractable. For simplicity, we take the MF approximation here to characterize the steady state of the system. In Appendix G, we compare MF with beyond-MF approximation methods to include the effects of correlations, namely, the MACEMF (see Appendix F 2) and cumulant-approximation methods. We show that at the atomic densities considered in this paper, the MF approximation is valid when describing the observables under consideration.

We obtain the MF equations of motion (see Appendix B) and express them as the Bloch equation, i.e., the same as Eq. (17), but here the components of the effective magnetic field, $\vec{B}_i^{\text{MF}}$ at atom i, are site dependent due to the inclusion of the dipolar interactions as

$$B_{i,x}^{\text{MF}} = \frac{\Omega}{2} + \frac{1}{4}\sum_{j\neq i}\left(\text{Re}\,\tilde{\mathcal{G}}_{ij}\langle\hat{\tilde{\sigma}}_j^x\rangle + \text{Im}\,\tilde{\mathcal{G}}_{ij}\langle\hat{\tilde{\sigma}}_j^y\rangle\right), \quad (21)$$

$$B_{i,y}^{\text{MF}} = \frac{1}{4}\sum_{j\neq i}\left(\text{Re}\,\tilde{\mathcal{G}}_{ij}\langle\hat{\tilde{\sigma}}_j^y\rangle - \text{Im}\,\tilde{\mathcal{G}}_{ij}\langle\hat{\tilde{\sigma}}_j^x\rangle\right), \quad (22)$$

$$B_{i,z}^{\text{MF}} = \frac{\Delta}{2}. \quad (23)$$

1. Short-time physics

Although the above MF treatment significantly reduces the complexity of the problem, the nonlinearity of these equations makes them difficult to solve analytically and apart from simple limiting cases, we need to solve them

numerically. The early-time dynamics ($\Gamma t \ll 1$) are one such regime in which it is possible to gain analytical insights.

To understand the role of interactions at short times, we include the inelastic interaction term in the Hamiltonian $\hat{H}$ [Eqs. (5) and (6)] and obtain the non-Hermitian Hamiltonian in the spiral basis as $\hat{H}_{\rm NH} = \hat{H} - i\sum_{k,j\neq k}\tilde{\mathcal{I}}_{kj}\hat{\tilde{\sigma}}_k^+\hat{\tilde{\sigma}}_j^- = \hat{H}_0 - \sum_{k,j\neq k}\tilde{\mathcal{G}}_{kj}\hat{\tilde{\sigma}}_k^+\hat{\tilde{\sigma}}_j^-$, where $\hat{H}_0$ describes the laser drive. Given that the system is initialized in a state in which all the Bloch vectors are identical in the tilde basis, i.e., $\langle\hat{\tilde{\sigma}}_k\rangle \equiv \langle\hat{\tilde{\sigma}}\rangle$, at short times, each Bloch vector commutes with terms of the form $(\hat{\tilde{\sigma}}_k \cdot \hat{\tilde{\sigma}}_j)$, since $\sum_{k,j\neq k}\langle[(\hat{\tilde{\sigma}}_k \cdot \hat{\tilde{\sigma}}_j), \hat{\tilde{\sigma}}_i]\rangle \sim \sum_{j\neq i}\langle\hat{\tilde{\sigma}}_j\rangle \times \langle\hat{\tilde{\sigma}}_i\rangle \sim 0$.

The emergence of a density shift can be elucidated by adding such terms, $(\hat{\tilde{\sigma}}_k \cdot \hat{\tilde{\sigma}}_j)$, to $\hat{H}_{\rm NH}$ without altering the physics of the original system at short times as

$$\hat{\mathcal{H}} = \hat{H}_{\rm NH} + \frac{1}{4}\sum_{k,j\neq k}\mathrm{Re}\,\tilde{\mathcal{G}}_{kj}\,(\hat{\tilde{\sigma}}_k \cdot \hat{\tilde{\sigma}}_j), \tag{24}$$

which allows us to rewrite the real part of the new Hamiltonian as $\mathrm{Re}\,\hat{\mathcal{H}} = \hat{H}_0 + \frac{1}{4}\sum_{k,j\neq k}\mathrm{Re}\,\tilde{\mathcal{G}}_{kj}\hat{\sigma}_k^z\hat{\sigma}_j^z$ and, at the mean-field level, as $\mathrm{Re}\,\hat{\mathcal{H}}^{\rm MF} = -\sum_i \vec{\mathcal{B}}_i^{\rm MF}\cdot\hat{\tilde{\sigma}}_i$, where $\vec{\mathcal{B}}_i^{\rm MF} = \vec{B}_{\rm L} - (\delta_i/2)\hat{z} = \{\Omega/2, 0, \Delta/2 - \delta_i/2\}$ and $\delta_i = \sum_{j\neq i}\mathrm{Re}\,\tilde{\mathcal{G}}_{ij}\langle\hat{\sigma}_j^z\rangle/2$ is the interacting part of $\vec{\mathcal{B}}_i^{\rm MF}$. This acts as a self-adjusting magnetic field along $\hat{z}$ that depends on the atomic inversion, $\langle\hat{\sigma}_j^z\rangle$. This effective field generated by other atoms in the array leads to a precession of each atomic dipole i about the $\hat{z}$ axis of the Bloch sphere, generating what is known as a density shift or a collective Lamb shift [75]. As the number of atoms in the cloud is increased, with the spatial extent fixed, the cloud gets denser and the induced frequency shift at each atom gets larger. The frequency shift has two components—a homogeneous component, $\Delta_{\rm MF}$, which is the average shift across atoms, and an inhomogeneous component, associated with the random distribution of the atoms in the array. The homogeneous component is nonzero when the cloud is not spherically symmetric and it pushes the atoms out of resonance, suppressing the growth of coherences and the excitation fraction. The inhomogeneous component leads to dephasing. These two key features will be an important consideration when we derive a simplified model of the dipolar Hamiltonian in Sec. IV.

The average frequency shift can be measured in Rabi spectroscopy by scanning the detuning for the new resonance condition, i.e., $\Delta_{\rm MF} = \sum_i \delta_i/N = \sum_{i,j\neq i}\mathrm{Re}\,\tilde{\mathcal{G}}_{ij}\langle\hat{\sigma}_j^z\rangle/(2N)$, where the right-hand side has been averaged over all atoms i [75]. The density shift can also be measured via Ramsey spectroscopy [76]. In this case, even at $\Delta = 0$, there is a residual precession that leads to a nonzero $\langle\hat{\tilde{S}}_x\rangle$ during the dynamics of the system, even when the system is initialized with $\langle\hat{\tilde{S}}_x\rangle = 0$. This feature distinguishes the dipolar model from the CRF and noninteracting models, where $\langle\hat{\tilde{S}}_x\rangle = 0$ at all times.

2. Weak-driving limit

Another simplified case is when the laser drive is very weak, $\Omega \ll \Gamma$, such that individual dipoles remain close to the south pole of the Bloch sphere, i.e., $\langle\hat{\sigma}_j^z\rangle \approx -1$, even in the steady state. In this regime, correlations are suppressed by factors of Ω/Γ and the system can be described almost exactly using mean-field theory by setting $\langle\hat{\sigma}_j^z\rangle = -1$ at all times and only considering the dynamics of the coherences $\langle\hat{\tilde{\sigma}}_j^+\rangle$. This regime has been intensively studied for dilute samples of dipolar-interacting atomic gases [12,17,18,20,21,24,28–31,36].

In the weak-driving limit ($\langle\hat{\sigma}_j^z\rangle = -1$) of our pencil-shaped Gaussian cloud, the average frequency shift is nonzero and, as discussed above, can be obtained at short times as $\Delta_{\rm MF} = -\sum_{j\neq i}^{N}\mathrm{Re}\,\tilde{\mathcal{G}}_{ij}/(2N)$. In the far-field limit ($|r_{ij}| \gg \lambda \Rightarrow \tilde{\mathcal{G}}_{ij} \propto 1/|r_{ij}|$), we find that $\sum_{j\neq i}^{N}\mathrm{Re}\,\tilde{\mathcal{G}}_{ij}/(2N) \propto N$, with a small ($\ll\Gamma$) proportionality constant that depends on the cloud extent and can be estimated numerically (for details, see Appendix D).

In the weak-driving limit, the mean-field steady-state coherence can also be obtained for a dilute gas by treating the interactions perturbatively as [17,30]

$$\langle\hat{\tilde{\sigma}}_j^-\rangle = \frac{i\Omega/2}{i\Delta + \Gamma/2}\left[1 - \frac{i}{i\Delta + \Gamma/2}\sum_{k\neq j}\tilde{\mathcal{G}}_{jk}\right] \tag{25}$$

and the forward intensity is obtained as

$$\frac{I(\vec{k}_{\rm L})}{I_0(\vec{k}_{\rm L})} = \frac{N(N-1)\Omega^2}{4\Delta^2 + \Gamma^2} \times\left[1 - \frac{\sum_{j,k\neq j}\left(\Gamma\mathrm{Im}\,\tilde{\mathcal{G}}_{jk} - 2\Delta\mathrm{Re}\,\tilde{\mathcal{G}}_{jk}\right)}{(\Delta^2 + \Gamma^2/4)N}\right]. \tag{26}$$

The steady-state density shift and the linewidth broadening can be obtained from the lineshape as $\bar{\Delta} = -\sum_{j,k\neq j}\mathrm{Re}\,\tilde{\mathcal{G}}_{jk}/N$ and $\bar{\Gamma} = 2\sum_{j,k\neq j}\mathrm{Im}\,\tilde{\mathcal{G}}_{jk}/N$, respectively [17,30]. On resonance ($\Delta = 0$), the x component of the coherence is proportional to the density shift, $\langle\hat{\tilde{S}}_x\rangle/N = 2\Omega\bar{\Delta}/\Gamma^2$ and the forward intensity is reduced by the inhomogeneous broadening as

$$I(\vec{k}_{\rm L}) \propto N(N-1)(\Omega/\Gamma)^2(1 - 2\bar{\Gamma}/\Gamma). \tag{27}$$

However, in a highly dense gas, multiphoton scattering processes become significant, making the steady state more complicated and beyond the perturbative limit [30].

B. Dynamical regimes in the steady state

Outside the special limits discussed above, we resort to numerical solutions for obtaining the steady state of the system. We find that our system exhibits different dynamical behaviors characterized by distinct light-emission properties, as we vary the laser driving strength Ω. Here, we draw parallels and distinctions among the steady-state properties of the dipolar, the noninteracting, and the CRF models, across different driving regimes.

1. Inversion, forward intensity, and two-photon correlation function

In Fig. 5(a), we show the atomic inversion of the dipolar model across a range of values of Ω. For the values of N explored in this work, we do not observe a phase transition in the dipolar model. Nevertheless, we find it is still useful to define a "critical" driving strength, $\Omega_C^{\text{dipolar}}$, for the dipolar model, as the drive strength at which the forward intensity, $\langle \hat{\tilde{S}}_+ \hat{\tilde{S}}_- \rangle$, peaks for a given N. The intensity peak separates the dynamical behaviors in the different driving regimes based on their emission properties, similar to the CRF model.

Note that our findings are distinct from the case of translationally invariant ordered arrays driven with a laser wave

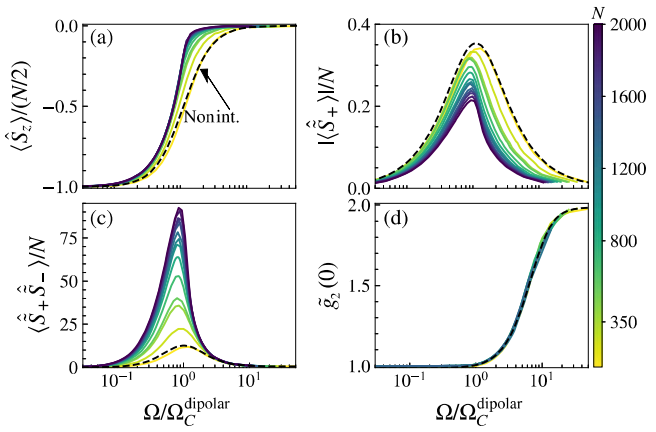

FIG. 5. The steady state of the MF dipolar model: (a) the atomic inversion, $\langle \hat{S}_z \rangle/(N/2)$; (b) the contrast, $|\langle \hat{S}_+ \rangle|/N$; (c) the "forward" intensity (along the axial direction); (d) the two-photon correlation function $\tilde{g}_2(0)$ in the "forward" direction. The dipolar model (solid line) converges to the noninteracting model (dashed black line) in the dilute limit (small N). The x axis of the noninteracting curve is scaled as $\Omega/\Omega_C^{\text{nonint.}} \sim \mathcal{O}(1)$ in (a)–(c) and as $\Omega/\Omega_C^{\text{dipolar}} \propto 1/\sqrt{N}$ in (d). In (a), (b), and (d), the noninteracting curve is independent of N; in (c), the noninteracting curve is for $N = 100$.

vector perpendicular to the array, where it has recently been predicted that, in the large-N limit, the system may undergo a first-order phase transition accompanied by bistability [54]. This prediction is nevertheless not in contradiction with our work, as Ref. [54] shows that even a "weak" disorder in the atomic positions can suppress bistability due to a reduction of the effective interaction strength. The system considered by us exhibits a large degree of disorder, lacks translational invariance, and as such eludes an analytical solution of the full MF equations. To enable some degree of analytical understanding, we instead introduce a set of simplifications, which despite not being totally rigorous, still capture the most relevant physics of the problem at hand and allow us to gain valuable physical insights. We discuss them later in Sec. IV.

We obtain $\Omega_C^{\text{dipolar}} = c\Gamma\sqrt{N}$ ($c \approx 0.08$) from the numerical steady state of the system. By plotting the steady-state atomic inversion as a function of a normalized drive strength, $\Omega/\Omega_C^{\text{dipolar}}$, we observe that the curves for different values of N appear to collapse, as shown in Fig. 5(a).

As N decreases, the cloud becomes dilute and the dipolar-interaction coefficients become less important. At very small N, the steady state of the noninteracting model is smoothly recovered for all the observables, as shown in Fig. 5.

In Fig. 5(c) of the dipolar model, we show that the variation of the forward intensity $\propto \langle \hat{\tilde{S}}_+ \hat{\tilde{S}}_- \rangle$ curve with the normalized drive strength is very similar to that of the noninteracting model [Fig. 4(c)]. The main difference between these two models is evident in the N scaling of $\langle \hat{\tilde{S}}_+ \hat{\tilde{S}}_- \rangle$. In the weak-driving regime of the CRF and noninteracting models, where phase matching leads to a perfect N^2 enhancement, we show that the forward-intensity curves for different values of N collapse when divided by N^2, in Figs. 3(c) and 4(c), respectively. But for the dipolar model, we find that the curves do not collapse when divided by N^2. At weak driving intensities, the site-dependent shifts due to the dipolar interactions imprint random phases on the coherences and thereby suppress the N^2 enhancement of $\langle \hat{\tilde{S}}_+ \hat{\tilde{S}}_- \rangle$ [30,36]. Hence, the N scaling of $\langle \hat{\tilde{S}}_+ \hat{\tilde{S}}_- \rangle$ decreases as N increases, as later shown in Fig. 8(b).

To further understand the emission properties of the steady state, we look at the forward two-photon correlation function $\tilde{g}_2(0) = \langle \hat{\tilde{S}}_+ \hat{\tilde{S}}_+ \hat{\tilde{S}}_- \hat{\tilde{S}}_- \rangle / \langle \hat{\tilde{S}}_+ \hat{\tilde{S}}_- \rangle^2$. As shown in Fig. 5(d), in the weak-driving regime ($\Omega \ll \Omega_C^{\text{dipolar}}$), we have $\tilde{g}_2(0) \approx 1$, which corresponds to a coherence state. This is expected because the steady state of the system resembles a coherent state on the Bloch sphere with a finite coherence $|\langle \tilde{S}_+ \rangle|/N$, as seen in Fig. 5(b) and later validated analytically using a simpler model (Sec. IV). Given that the CRF, noninteracting, and dipolar models all feature almost pure Gaussian-like steady states in this regime, $\tilde{g}_2(0)$ is not

able to distinguish their subtle differences and all the three models have $\tilde{g}_2(0) \sim 1$ in the weak-excitation limit [see Figs. 3(d), 4(d), and 5(d)].

When the drive strength is above the "critical" level, i.e., $\Omega \gg \Omega_C^{\text{dipolar}}$, the drive quickly dephases the array. As a consequence, dipolar interactions become subdominant compared to the rapid rotation induced by the drive. Consistently, the steady state starts to become fully mixed, with suppressed coherences, signaled by the fact that $\tilde{g}_2(0) \sim 2$ approaches its thermal value [see Fig. 5(d)].

This is in stark contrast to the CRF case, where the collective nature of the master equation enforces the preservation of the collective nature of the state even in the large-driving limit ($\Omega \gg \Omega_C^{\text{CRF}}$). Therefore, the intensity keeps scaling as N^2 [Eq. (15)], as shown in Fig. 3(c), and $\tilde{g}_2(0)$ remains always below the thermal value and saturates as $\tilde{g}_2(0) \to 1.2$ [see Fig. 3(d)]. These key distinctions imply that a free-space atomic cloud does not behave as a CRF model in the strong-driving regime.

2. *Steady-state frequency shift and contrast*

In Fig. 6(a), we see that the steady state of the dipolar model has $\langle \hat{\tilde{S}}_x \rangle \neq 0$, unlike the noninteracting [Fig. 4(b)] and CRF [Fig. 3(b)] models, where the x component of the collective coherence is zero. The resonant laser drive commutes with $\langle \hat{\tilde{S}}_x \rangle$ and the finite $\langle \hat{\tilde{S}}_x \rangle$ arises from the dispersive (elastic) part of the dipolar interactions, which leads to frequency shifts, as discussed in Sec. III A. The latter is most prominent in the weak-driving limit, where the inversion remains close to its initial minimum value. In this limit, the fractional x component of the coherence, $|\langle \hat{\tilde{S}}_x \rangle|/|\langle \hat{\tilde{S}}_+ \rangle|$, increases with N, which suggests that denser clouds have larger collective shifts.

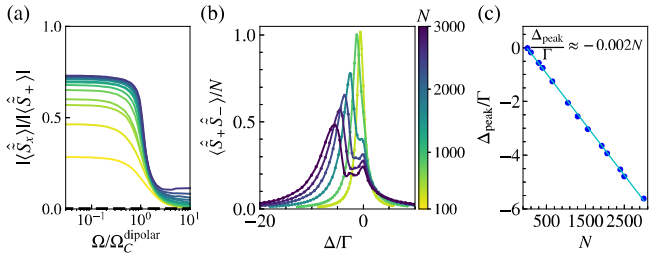

FIG. 6. (a) The x component of the coherence, $|\langle \hat{S}_x \rangle|/|\langle \hat{S}_+ \rangle| \neq 0$, arising from frequency shifts due to the elastic dipolar interactions. For the noninteracting model, $\langle \hat{\tilde{S}}_x \rangle = 0$ (dashed black line). (b) The steady-state "forward" intensity for a range of laser detunings, Δ: the dots show the MF-dipolar-model numerics, while the solid lines show the interpolated data. (c) The steady-state frequency shift, computed as the detuning at which the maximum intensity is reached (circles), which follows a linear dependence with N, as can be seen from the linear best fit (solid line). Data from numerics of the MF dipolar model in the weak-driving regime ($\Omega/\Gamma = 0.1$), averaged over ten realizations.

Beyond the critical drive, as shown in Fig. 5(b), the contrast, $|\langle \hat{\tilde{S}}_+ \rangle| = \sqrt{\langle \hat{\tilde{S}}_x \rangle^2 + \langle \hat{\tilde{S}}_y \rangle^2}$, starts decaying as the state begins to get mixed and the Bloch-vector length gets smaller. This behavior continues with increasing Ω/Γ until eventually the Bloch vector of the system reduces to the one expected for the noninteracting system. The approach to the noninteracting regime as the system reaches the strong-driving regime is also signaled by the dominant $\langle \hat{\tilde{S}}_{y,z} \rangle$ spin projections and the reduced $\langle \hat{\tilde{S}}_x \rangle$ one. This in turn leads to a reduced value of $|\langle \hat{\tilde{S}}_x \rangle|/|\langle \hat{\tilde{S}}_+ \rangle|$, as shown in Fig. 6(a).

In Fig. 6(b), we look at the lineshape of the steady-state intensity in the weak-driving regime ($\Omega/\Gamma = 0.1$) by varying the laser detuning, Δ, of the MF dipolar model. We find that increasing N leads to a bimodal distribution with a peak at $\Delta = 0$ and a second resonance at Δ_{peak}. Note that the second peak arises from dipolar interactions and scales linearly with N, as shown in Fig. 6(c).

The linear N scaling is consistent with previous work done in the weak-driving limit [17,30,36,77,78] that has observed a frequency shift proportional to the atomic density. In our quasi-one-dimensional (quasi-1D) configuration along the $\hat{x}$ axis, the atomic density scales as $\rho \sim N/(a_{ho}^2 L)$, where $L = 2l_{\text{ax}}$ is the axial length of the pencil-shaped cloud and $a_{ho} \ll x_{ij}$ sets the radial confinement. The existence of a prominent second peak can be naively understood from the fact that the inter-atomic distances are determined by the axial spacing, i.e., $k_0|\vec{r}_{ij}| = k_0\sqrt{x_{ij}^2 + y_{ij}^2 + z_{ij}^2} \approx k_0|x_{ij}|$. As such, the pairwise interactions between atoms along the $\hat{x}$ axis contribute constructively to the shift. Mathematically, this is because the phases imprinted by the laser cancel those of the Green's function, $\tilde{\mathcal{G}}_{i>j} \propto \exp(ik_0|\vec{r}_{ij}| - i\vec{k}_{\text{L}} \cdot \vec{r}_{ij}) \sim 1$ (for more details, see Appendix B). Hence, by aligning the laser wave vector along the elongated geometry of the cloud, one can induce a nonzero global frequency shift even in a disordered configuration [23].

As discussed earlier in Sec. III A 2, the steady-state density shift of the lineshape in the weak-driving limit for a dilute gas is $\bar{\Delta} = -\sum_{k \neq j} \text{Re}\,\tilde{\mathcal{G}}_{jk}/N$. For simplicity, we consider the far-field regime ($\propto 1/r$) of the interactions, which is the dominant term in the dilute case, and obtain $\bar{\Delta}$ in the large-N limit by integrating over the pencil-shaped distribution of the cloud, as $\bar{\Delta} = -c_{\text{R}} N\Gamma$, where $c_{\text{R}} \approx 0.003$ is a constant depending on the spatial extent of the cloud. Similarly, we obtain the linewidth broadening as $\bar{\Gamma} = c_{\text{I}} N\Gamma$ with $c_{\text{I}} \approx 0.004$. In the regime in which $2\bar{\Gamma} > \Gamma$, i.e., $N > 250$, the dilute gas description is no longer valid on resonance as, under this assumption, the predicted forward intensity becomes unphysical [Eq. (27)]

and the perturbative treatment fails. Thus, even though the prediction of $\bar{\Delta}$ is very close to Δ_{peak}, the weak-driving physics in our system is beyond the first-order expansion in interactions.

Of course, our analysis neglects motional effects in thermal samples, laser forces, and dipolar forces. As shown in Ref. [30], motional decoherence can induce a reduction of the density shift and wash out the double-peak structure compared to what is expected for frozen atoms.

C. N scaling for different driving strengths

To emphasize the collapse of the curves for different values of N and the different critical properties across models, we compare the steady-state atomic inversion across a wide range of driving strengths for the dipolar model (solid line), the CRF model (dashed-dotted line), and the noninteracting model (dotted line), in Fig. 7(a). The x axis of Fig. 7(a) has been scaled differently for each model, corresponding to the scaling of the "critical" driving strength Ω_C^m, where $m \in$ {CRF model, Dipolar model, Nonint. (Noninteracting) model}. The N scaling of Ω_C^m for these models has been shown in Fig. 7(b). The N scaling of the critical drive for the dipolar model ($\propto \sqrt{N}$) clearly differs from that of the noninteracting [approximately $\mathcal{O}(1)$] and CRF ($\propto N$) models.

In Fig. 8, we show the N scaling of the steady-state intensity, i.e., we define $\alpha(\Omega/\Gamma, N)$ such that $I(\vec{k}_L) \propto \langle \hat{\tilde{S}}_+ \hat{\tilde{S}}_- \rangle \propto N^{\alpha(\Omega/\Gamma, N)}$ at fixed Ω/Γ, across a wide range of driving strengths. Note that $\alpha(\Omega/\Gamma, N)$ varies slowly with N and we obtain $\alpha(\Omega/\Gamma, N)$ by fitting the steady-state intensity to a power law over a finite range, $[N - \delta N, N]$, $\delta N \sim 0.4N$. In Fig. 8(a), we choose the x axis to be the bare driving strength Ω/Γ, to compare our predictions with the measurements of a recent experiment [61]. In the weak-driving regime, we find $\alpha < 1$ for the dipolar and

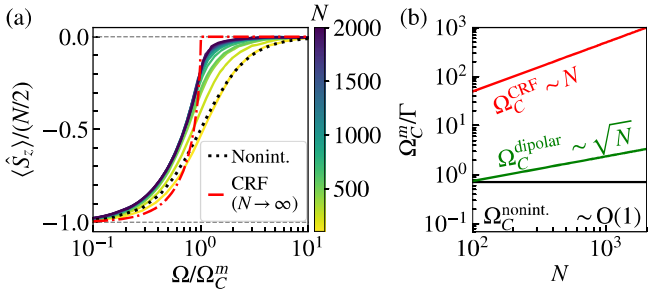

FIG. 7. (a) The steady-state atomic inversion $\langle \hat{S}_z \rangle/(N/2)$ for the dipolar (solid line), noninteracting (dotted line), and CRF (dashed-dotted line) models. The x axis is scaled with the critical drive Ω_C^m for each model, m. (b) The N scaling of Ω_C^m for the dipolar (approximately $\sqrt{N}$), noninteracting (approximately $\mathcal{O}(1)$), and CRF (approximately N) models.

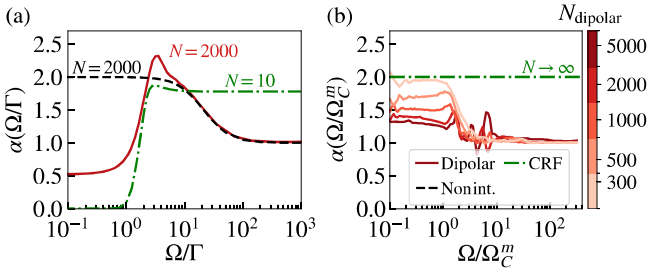

FIG. 8. The N-scaling exponent of the steady-state "forward" intensity, $\langle \hat{\tilde{S}}_+ \hat{\tilde{S}}_- \rangle \propto N^\alpha$. (a) α computed at a fixed Rabi frequency, Ω/Γ, similar to Ref. [61]. α is similar for the CRF ($N = 10$) and dipolar model ($N = 2000$) in the intermediate-driving regime for a small range of Ω/Γ, which has been probed in Ref. [61]. At large Ω/Γ, $\alpha = 2$ for the CRF due to the preservation of $\langle \hat{\mathbf{S}}^2 \rangle$ but the dipolar model becomes single-particle-like ($\alpha = 1$) due to spontaneous emission. Due to finite-size effects, $\alpha < 2$ for $N = 10$ (CRF). (b) α computed at a fixed Ω/Ω_C^m, the ratio of the Rabi frequency and the critical drive, for each model: MF dipolar (solid lines), noninteracting (dashed black line), and CRF (dashed-dotted green line).

the CRF models. Usually, $\alpha < 1$ is understood as a signature of subradiance but in our case this is simply an artifact due to the N scaling being calculated at a fixed bare driving strength, Ω/Γ. At a fixed value of Ω/Γ, the system crosses over from the strong—($\Omega \gg \Omega_C^{\text{dipolar}}, \Omega \gg \Omega_C^{\text{CRF}}$) to the weak—($\Omega \ll \Omega_C^{\text{dipolar}}, \Omega \ll \Omega_C^{\text{CRF}}$) driving regime as N is increased, leading to an inaccurate N scaling. The dependence of $\alpha(\Omega/\Gamma, N)$ on N also arises because increasing N at a fixed Ω/Γ changes the physical regime. The variation of $\alpha(\Omega/\Gamma, N)$ with N is most apparent when N approaches the value at which $\Omega \sim \Omega_C^{\text{dipolar}}$ and the system crosses over from the weak to the strongly driven regime. This leads to a "kink" in α, i.e., $\alpha > 2$, for the mean-field dipolar model at intermediate driving strengths in Fig. 8(a), which is again an artifact of fixing Ω/Γ. These artifacts are not seen for the noninteracting model because $\Omega_C^{\text{nonint.}} \sim \mathcal{O}(1)$ (in the large-N limit), so fixing Ω/Γ also fixes the regime for all N.

In Fig. 8(a), we see that α of the dipolar model coincides with that of the noninteracting model in the regime of strong driving for all $N \leq 2000$, i.e., $\Omega \gg \Omega_C^{\text{dipolar}} = c\Gamma\sqrt{N} \approx 3.6\Gamma$. This confirms our expectation that in the strong-driving regime, the dipolar model behaves like the noninteracting model. In Fig. 8(a), we also see the clear difference between the CRF and the dipolar models in the strong-driving regime. We show the CRF model for $N = 10$ to compare with the experimental prediction [61], where it is reported that a cloud of $N = 2000$ atoms can equivalently be described by the CRF model of a reduced effective atom number, $N_{\text{eff}} = 10$. Close to the peak, the α of the dipolar model agrees with that of the CRF model

in a small range of Ω/Γ. Even though the two models have very different α in general, this was the regime probed by the experiment, partly justifying the conclusions drawn in Ref. [61]. Reaching the genuine strong-driving limit requires large enough Rabi frequencies, which are not so accessible in current experiments.

In Fig. 8(b), we calculate the N scaling by properly fixing the scaled driving strength, $\Omega/\Omega_C^{\text{dipolar}}$ and, as expected, we find no signatures of subradiance. Moreover, the divergence of α, i.e., the region in which $\alpha > 2$, seen in Fig. 8(a), vanishes. Instead, at weak driving, $\alpha(\Omega/\Omega_C^{\text{dipolar}}, N)$ decreases from 2 (perfect phase matching) to close to 1 (randomized phases) for the dipolar model as N is increased and the collective shifts get stronger, suppressing the N^2 enhancement. In the weak-driving regime, the variation of $\alpha(\Omega/\Omega_C^{\text{dipolar}}, N)$ with N arises from the fact that at small N, the system is dilute and behaves as the noninteracting model with perfect phase matching ($\alpha \approx 2$). As N is increased, the interactions get stronger and the interaction-induced dephasing suppresses the phase matching more and more, thus reducing α. Furthermore, even within a given driving regime, α can vary due to the finite size of the system. At larger N, the dynamical behavior of the system begins to converge with increasing N and therefore α varies more slowly, approaching a fixed N-independent value. In the strong-driving regime, $\alpha \to 1$ for all N, as the system becomes single-particle-like. We show the best fits for extracting α for different values of N in Sec. B 1. On the other hand, for the CRF model, in the large-N limit, α scales as N^2 in all driving regimes.

IV. MODIFIED-CRF (Mod-CRF) MODEL

In this section, we propose a simplified theoretical model at the mean-field level to describe the emergent properties of our system. In the microscopic picture of the dipolar model, the dispersive part of the dipole-dipole interactions between atoms leads to a frequency shift in the transition frequency of each atom, as discussed in Sec. III A. This shift can equivalently be captured by an additional term $\sum_{i=1}^{N} \delta_i(t)\hat{\sigma}_i^z$ in the CRF Hamiltonian, as

$$\hat{H}_{\text{Mod-CRF}} = -\Omega\hat{S}_x + \sum_{i=1}^{N} \delta_i(t)\hat{\sigma}_i^z, \tag{28}$$

where the frequency shift of an atom i is described as $\delta_i(t) = \sum_{j\neq i} \text{Re}\,\tilde{\mathcal{G}}_{ij}\langle\hat{\sigma}_j^z(t)\rangle/4$, inspired by the short-time dynamics of the MF dipolar model. To distinguish the collective slowly varying part of the interaction-induced shift from the inhomogeneous fast time-varying effects, we express the frequency shift as $\delta_i(t) = \bar{\delta}(t) + h_i(t)$, where $\bar{\delta}(t) = \sum_{i,j\neq i} \text{Re}\,\tilde{\mathcal{G}}_{ij}\langle\hat{\sigma}_j^z(t)\rangle/(4N)$ is the average shift across all the atoms in the cloud at any time t and $h_i(t)$ is the fast time-varying inhomogeneous component, which describes beyond-short-time dynamics. The homogeneous component, $\bar{\delta}(t)$, is dominated by the shifts that add up along the axial direction due to the constructive interference of the laser-induced phases with the interaction-induced phases. To capture the constructive shifts in a simplified way, we assume that $\bar{\delta}(t)$ for our cloud can be described by a collective system, such as a translationally invariant atomic array, giving $\bar{\delta}(t) \approx \sum_i \text{Re}\,\tilde{\mathcal{G}}_{i0}\langle\hat{S}_z(t)\rangle/(2N)$. The interaction-induced time-varying inhomogeneous component, $h_i(t)$, accounts for the random and dynamic evolution of the atomic dipolar phases. $h_i(t)$ has a zero mean, is time dependent, and is therefore not removable by a simple echo pulse. For simplicity, these conditions are roughly incorporated by considering the h_i functions as stochastic white-noise variables with spectral function: $\overline{h_i(t)h_j(t')} = 4\gamma_d\delta_{ij}\delta(t-t')$ [79].

The net dephasing arising from the $h_i(t)\hat{\sigma}_i^z$ term can be accounted for by local jump operators $\sqrt{\gamma_d}\hat{\sigma}_i^z$ in the master-equation formulation, where γ_d is a common dephasing rate for all the atoms, which we set to be proportional to the variance of the frequency shifts (for details, see Sec. D 1), which scales linearly with the density of the atomic ensemble [5,17,30]. Thus, we define the dephasing rate as $\gamma_d = c_d N\gamma_s$, where c_d is a phenomenological constant that depends on the overall volume and geometry of the atomic cloud and γ_s is the spontaneous-emission decay rate.

Accounting for the overall elastic interactions, the collective superradiant emission from nearby atoms, and the single-particle spontaneous emission (since the purely collective behavior is only possible in the high-density limit, not achieved in the experiment), we obtain the modified CRF model described by a master equation of the form $\dot{\hat{\rho}} = -i[\hat{H}_{\text{mod-CRF}}, \hat{\rho}] + \mathcal{L}_{\text{mod-CRF}}(\hat{\rho})$, where the Hamiltonian is

$$\hat{H}_{\text{mod-CRF}} = -\Omega\hat{S}_x + \chi\langle\hat{S}_z\rangle\hat{S}_z, \tag{29}$$

where $\chi = 2\bar{\delta}(t)/\langle\hat{S}_z(t)\rangle = \sum_{i\neq 0} \text{Re}\,\tilde{\mathcal{G}}_{i0}/N$ is a constant. $\chi\langle\hat{S}_z(t)\rangle$ acts as a time-dependent global magnetic field, which describes the shearing of the collective Bloch vector via one-axis twisting (OAT) at the mean-field level. The Lindbladian is expressed as

$$\begin{aligned}\mathcal{L}_{\text{mod-CRF}}(\hat{\rho}) = {}& \frac{\Gamma_D}{2}\left(2\hat{S}_-\hat{\rho}\hat{S}_+ - \{\hat{S}_+\hat{S}_-, \hat{\rho}\}\right) \\ & + \frac{\gamma_s}{2}\sum_j\left(2\hat{\sigma}_j^-\hat{\rho}\hat{\sigma}_j^+ - \{\hat{\sigma}_j^z, \hat{\rho}\}/2 - \hat{\rho}\right) \\ & + \gamma_d\sum_j\left(\hat{\sigma}_j^z\hat{\rho}\hat{\sigma}_j^z - \hat{\rho}\right),\end{aligned} \tag{30}$$

where the first line is the collective dissipation in the CRF model with rate $\Gamma_D = \sum_{j\neq 0} \mathrm{Im}\,\tilde{\mathcal{G}}_{0j}/N$, the second line is the single-particle spontaneous emission with decay rate γ_s, and the third line is the single-particle dephasing with rate γ_d. Unlike the CRF model, this modified model does not preserve $\langle \hat{\mathbf{S}}^2 \rangle$. The case without dephasing ($\gamma_d = 0$) and OAT ($\chi = 0$) has been predicted to show a first-order phase transition and bistability [57,71,80] at a critical driving strength given by $\Omega_C \approx \Gamma_D N/(2\sqrt{2})$. Hence, spontaneous emission only changes the critical drive by a factor of $1/\sqrt{2}$ compared to the original CRF model ($\Omega_C{}^{\mathrm{CRF}} = \Gamma N/2$). When we include the effect of dephasing ($\gamma_d \neq 0$) and dispersive interactions ($\chi \neq 0$), we find that the modified model still undergoes a first-order phase transition with bistability but the critical point depends on the N scaling of γ_d. We obtain the mean-field steady state in the superradiant phase for $N \gg 1$ from the following self-consistent equations (for a derivation, see Appendix D):

$$\frac{\langle \hat{S}_z \rangle}{N/2} = -\frac{1}{2} \pm \frac{1}{2}\sqrt{1 - 8\left(1 + \frac{4\gamma_d}{\gamma_s}\right)\left(\frac{\langle \hat{S}_x \rangle^2 + \langle \hat{S}_y \rangle^2}{N^2}\right)}, \tag{31}$$

$$\frac{\langle \hat{S}_x \rangle^2 + \langle \hat{S}_y \rangle^2}{N^2} = \frac{\Omega^2 - \Gamma_D \gamma_s N(1 + \langle \hat{S}_z \rangle/(N/2))}{N^2(\Gamma_D^2 + \chi^2)}. \tag{32}$$

The critical point is defined as the driving strength at which the above solution ceases to be valid and is obtained as (with $\gamma_d = c_d N \gamma_s/4$)

$$\Omega_C^{\text{mod-CRF}} = \Gamma_D \sqrt{N} f \tag{33}$$

where $f \approx \frac{1}{2\sqrt{2}}\sqrt{\{[1 + (\chi/\Gamma_D)^2]/c_d\} + (4\gamma_s/\Gamma_D)}$ is a constant.

In Fig. 9, we show the steady-state values of the Mod-CRF model obtained from mean-field numerics, where we have set $c_d = 0.002$. This specific value of c_d is not special and we find qualitatively similar results for other values as long as $c_d \ll 1$. We have $\chi = \sum_{j\neq 0} \mathrm{Re}\,\tilde{\mathcal{G}}_{0j}/N \approx 0.003$ and $\Gamma_D = \sum_{j\neq 0} \mathrm{Im}\,\tilde{\mathcal{G}}_{0j}/N \approx 0.002$ for our pencil-shaped cloud (for details, see Appendix D). The steady state of the Mod-CRF model shows qualitatively similar behaviors to the MF dipolar model (Fig. 5). The critical drive strength for the Mod-CRF model, $\Omega_C^{\text{mod-CRF}}$, scales as approximately $\sqrt{N}$, similar to $\Omega_C^{\text{dipolar}}$. This $\sqrt{N}$ scaling is also recovered in the numerics as the scaled numerical curves (x-axis scaling $\Omega/\Omega_C^{\text{mod-CRF}}$) of the atomic inversion become indistinguishable at large N [Fig. 9(a)]. Similarly, the scaled numerical curves of the intensity [Fig. 9(c)], $g_2(0)$ [Fig. 9(d)], and the atomic coherences [Figs. 9(b) and 9(e)] also look indistinguishable. In the weak-driving regime, the real part of the atomic coherence, $\langle \hat{S}_x \rangle$, is nonzero and increases with N due to collective shifts [Fig. 9(e)]. In the strong-driving regime ($\Omega \gg \Omega_C^{\text{mod-CRF}}$), the intensity of the Mod-CRF becomes single-particle-like, i.e., $\langle \hat{S}_+ \hat{S}_- \rangle = N/2$, as the coherences go to zero [Fig. 9(b)]. In this regime, the atomic inversion goes to zero as well [Fig. 9(a)] and $g_2(0)$ reaches its thermal value of 2 [Fig. 9(d)]. These characteristics describe a departure from the CRF model and qualitatively resemble the properties of the MF dipolar model [Figs. 5 and 6(a)].

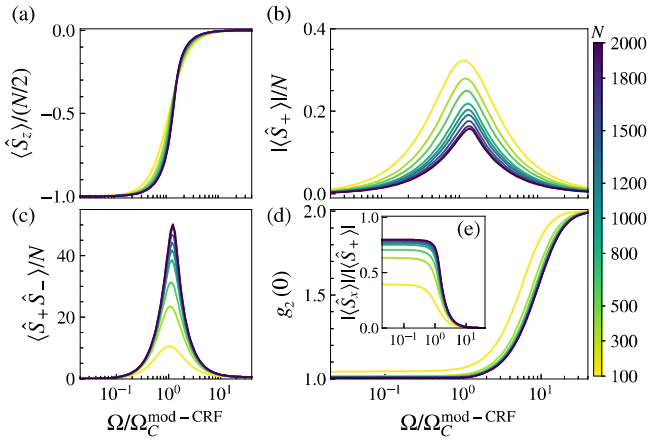

FIG. 9. (a)–(d) The steady state of the modified CRF model from MF numerics: (a) the atomic inversion $\langle \hat{S}_z \rangle/(N/2)$; (b) the total coherence, $|\langle \hat{S}_+ \rangle|/N$; (c) the intensity $\langle \hat{S}_+ \hat{S}_- \rangle$, which largely scales as approximately N due to dephasing; (d) the two-photon correlation function $g_2(0)$. (e) The x component of the coherence, $|\langle \hat{S}_x \rangle|/|\langle \hat{S}_+ \rangle| \neq 0$, arising from the mean-field frequency shift. In the large-N limit, $\Omega_C^{\text{mod-CRF}} \sim \Gamma\sqrt{N}$ is the critical drive for this model [Eq. (33)].

While the analytically obtained steady-state atomic inversion in Eq. (31) can feature bistability and undergo a first-order transition, we do not observe these features in Fig. 9(a). This is owing to the values of the model parameters, which are the ensemble averages of the original dipolar coefficients. These parameters are consistent with the experimental densities, where the far-field ($1/r$) interactions dominate the physics and MF is valid. In particular, at the densities considered in our work, we have $\Gamma_D N \sim \gamma_d$, i.e., the collective decay and the dephasing rates are similar in value. The competition between collective decay and dephasing determines how collective the system remains and the sharpness of the phase transition. As the collective decay rate is increased beyond that used in Fig. 9, we find that the bistability starts to become more prominent. However, we believe that at such large densities, the MF model becomes invalid and beyond-MF corrections arising from the strong near-field ($1/r^3$) interactions dominate the physics, leading to correlations [81] as well as motional effects [30], all neglected so far in our analysis. Understanding the validity of an MF description in the high density regime, however, is beyond the scope

of our current study and is deferred to follow-up investigations. Here, we just limit ourselves to saying that while we cannot rule out the existence of a phase transition in the thermodynamic limit, from the numerical analysis carried out in the less dense regime relevant for current experiments, we do not expect a transition to happen. A rigorous investigation of the high density limit nevertheless remains an open question.

V. COMPARISONS WITH EXPERIMENT

In this section, we compare our mean-field numerics for the dipolar model with experimental results [61]. The experimental system and measurement protocols are all described in Ref. [61]. The participating states correspond to the σ_+-polarized atomic transition between the two levels $|5S_{1/2}, F = 2, m_F = 2\rangle \rightarrow |5P_{3/2}, F = 3, m_F = 3\rangle$ in ^{87}Rb with linewidth $\Gamma = 2\pi \times 6$ MHz. The Clebsch-Gordan coefficient for this transition is 1. This system is the same as the one described in Fig. 2.

In Fig. 10, we show the dynamics of the total excitation fraction $n_e(t) = \sum_i (\langle \hat{\sigma}_z^i(t)\rangle + 1)/(2N)$. To do this, we evolve the system under a continuous drive with Rabi frequency $\Omega = 4.5\Gamma$ from the ground state to the steady state. We find that the mean-field numerics (red lines) agree more or less with the experiment (blue traces), for different values of N. The red-shaded region shows n_e within a range of N values to account for experimental uncertainties. Both the numerics and the experimental data feature a dephasing of the Rabi oscillations with increasing particle number, which is not seen in the noninteracting model (dashed black line).

In Fig. 11(a), we look at the steady-state atomic inversion and find very good agreement of our numerics (continuous lines) with the experimental data (symbols) for $N = 300$. An experimental data point in Fig. 11(a) for $N = 1500$ at $\Omega/\Gamma \approx 4.5$ ($\langle \hat{S}_z\rangle/(N/2) \approx -0.45$) is not consistent with the steady state in Fig. 10(c) ($n_e(t \rightarrow \infty) \approx 0.5 \Rightarrow \langle \hat{S}_z\rangle/(N/2) \approx 0$). This could be due to calibration

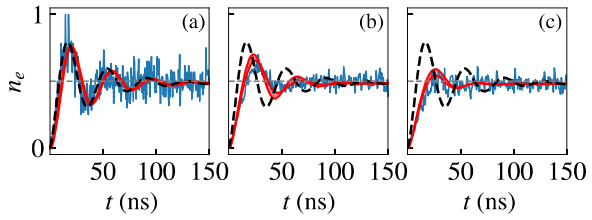

FIG. 10. The excitation fraction n_e versus time for fixed $\Omega/\Gamma = 4.5$—MF dipolar numerics for $N_{\rm MF}$ atoms (thick red line) on top of experimental data (blue traces) for $N_{\rm exp}$ taken from Ref. [61]: (a) $N_{\rm exp} = 350$, $N_{\rm MF} = 350$; (b) $N_{\rm exp} = 1000$, $N_{\rm MF} = 1150 \pm 13\%$; (c) $N_{\rm exp} = 1600$, $N_{\rm MF} = 1700 \pm 6\%$. The red-shaded regions show the numerics data in the specified $N_{\rm MF}$ ranges. The dashed black line is the solution of the noninteracting model.

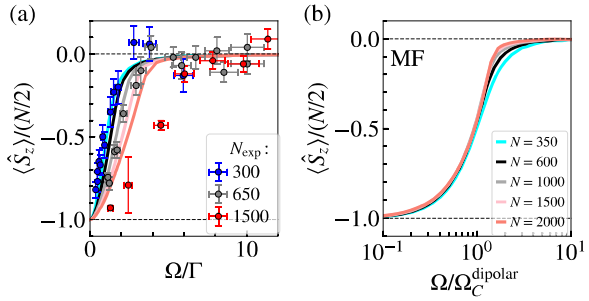

FIG. 11. $\langle \hat{S}_z\rangle/(N/2)$: the steady-state atomic inversion. (a) MF dipolar numerics (solid lines) and experimental data (symbols) from Ref. [61]. (b) MF data with x-axis scaling of approximately $\Omega/\Omega_C^{\rm dipolar}$, showing the collapse of curves for different values of N.

errors or other experimental systematics. Other than these quantitative differences, it is clear that there is a qualitative agreement with the theory in the trends observed in the experiment. In Fig. 11(b), we plot the numerical data with our scaling of the Rabi frequency, $\Omega/\Omega_C^{\rm dipolar} \sim \Omega/(0.08\Gamma\sqrt{N})$, and the data collapse to a single curve, as previously discussed. In Fig. 11(a), while the weakly driven regime begins to appear at values of $\Omega/\Omega_C^{\rm dipolar} < 1$, where $\langle \hat{S}_z\rangle/(N/2) \lesssim -1/2$, there are very few experimental data points in this regime, which may make it seem that the weakly driven limit is missing. To fully reach the weakly driven limit, $\langle \hat{S}_z\rangle/(N/2) \rightarrow -1$, smaller values of Ω are needed, as shown in Fig. 11(b), i.e., $\Omega/\Omega_C^{\rm dipolar} < 0.1$, which would amount to $\Omega < 0.3\Gamma$ for $N_{\rm exp} = 1500$ and $\Omega < 0.1\Gamma$ for $N_{\rm exp} = 300$. In the purely theoretical figure [Fig. 11(b)], with the x axis ($\Omega/\Omega_C^{\rm dipolar}$) scaled logarithmically, the weak-driving regime becomes more visible.

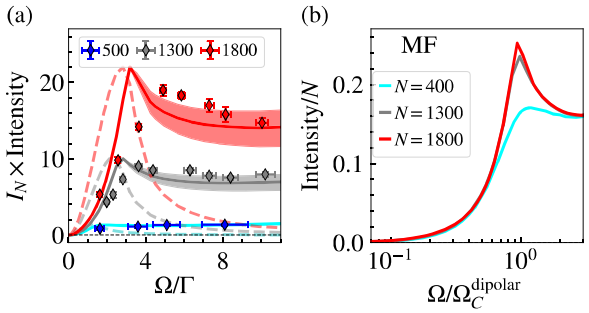

FIG. 12. (a) The steady-state intensity of the MF dipolar model in the forward direction ($\theta = 0$, dashed line), averaged over a solid angle ($\Delta\theta = \theta_{\rm out} - \theta_{\rm in}$) around the forward direction with $\theta_{\rm in} = \pi/22$ and $\theta_{\rm out} = \pi/7 \pm \pi/50$ (solid lines, shaded region), and experimental data (dots) from Ref. [61]. I_N is a fitting factor for the MF dipolar model, chosen to match the theory peak with the experimental values. (b) MF data ($\theta_{\rm in} = \pi/22$ and $\theta_{\rm out} = \pi/7$) with x-axis scaling $\sim\Omega/\Omega_C^{\rm dipolar}$ show the collapse of curves, as expected.

In Fig. 12(a), we compare the steady-state intensity from MF numerics with the experimental data [61] and find fair agreement. Here, we look at the steady-state intensity, $I_0(\vec{k})\sum_{ij}\langle\hat{\sigma}_i^+\hat{\sigma}_j^-\rangle e^{i\vec{k}\cdot\vec{r}_{ij}}$, strictly in the forward direction ($\vec{k}=\vec{k}_L$, dashed line) and averaged over a solid angle around the forward direction (shaded region). Here, $\hat{k}=\{\cos\theta,\sin\theta\cos\phi,\sin\theta\sin\phi\}$, is the direction of observation, with θ the angle from the $\hat{x}$ axis (forward direction) and ϕ the azimuthal angle in the y-z plane from $\hat{y}$. For the circularly polarized transition, $\hat{e}_q=\hat{e}_+=-(\hat{x}+i\hat{y})/\sqrt{2}$, and we obtain $I_0(\vec{k})\propto(1+\sin^2\theta\sin^2\phi)/2$ (see Appendix A 3). As some of the light in the forward direction is filtered out in the experiment to remove the laser light, we average the intensity over an annular region [30,82], such that the averaged intensity is expressed as $\int_{\theta_{in}}^{\theta_{out}}d\theta\int_0^{2\pi}d\phi\sin\theta I_0(\vec{k})\sum_{ij}\langle\hat{\sigma}_+\hat{\sigma}_-\rangle e^{i\vec{k}\cdot\vec{r}_{ij}}/A$, where $\theta_{out}=\pi/7\pm\pi/50$, $\theta_{in}=\pi/22$, and $A=\int_{\theta_{in}}^{\theta_{out}}d\theta\int_0^{2\pi}d\phi\sin\theta$ is the normalization factor. The values of θ_{out} and θ_{in} are extremely difficult to determine experimentally and hence we consider them as fitting parameters, while making sure that their values remain within a reasonable range.

Furthermore, we have included direct contributions from the probe light to the intensity, considering that the filter may not be perfect (for details, see Appendix E). We use an approximately 4% leakage of probe light intensity, which is also a fitting parameter, and its value is consistent across Figs. 12–14. The experimental data, which represent the photon rate in arbitrary units, are scaled with a fitting factor, which has been used in Ref. [61] to compare their data with the CRF model. To compare our results with the experimental data, we scale the intensity with a fitting factor I_N, which is obtained by matching the peak of the experimental curve with the peak of the numerics for each N.

In Fig. 13, we compare the dynamics of the forward intensity, $I(t)$, measured in the experiment (red traces) [83], with the intensity from the MF numerics in the strictly forward direction (dashed black line) and the MF numerics data averaged over a solid angle about the forward direction (solid blue line) with $\theta_{in}=\pi/22$ and a range of $\theta_{out}=\pi/7\pm\pi/50$ (blue-shaded region). This is the same range of solid-angle values as discussed earlier for the steady-state intensity. To properly compare the bare photon rate from the experiment with the numerical values of the intensity, we scale the dynamical intensity $I(t)$ by its steady-state value I_{SS}, thus making the scaled intensity, $I(t)/I_{SS}$, independent of the distance between the atomic cloud and the detector, which is difficult to determine exactly for the experimental setup. In the weak ($\Omega<\Omega_C^{dipolar}$) and intermediate ($\Omega\sim\Omega_C^{dipolar}$) driving regimes, the experiment agrees well with the purely forward intensity of the dipolar model (dashed black line) for different values of N, as shown in Figs. 13(a)–13(c). In Figs. 13(d)–13(f), we see that in the strong-driving regime ($\Omega>\Omega_C^{dipolar}$), the experiment agrees well with the dipolar-model intensity when averaged over the solid angle (blue-shaded region) for different values of N. Thus, the solid angle $(\theta_{in},\theta_{out})$, for which the numerics and the experiment agree, depends on the drive strength, Ω/Γ. One possible explanation is the fact that the radiative force of the laser pushes the

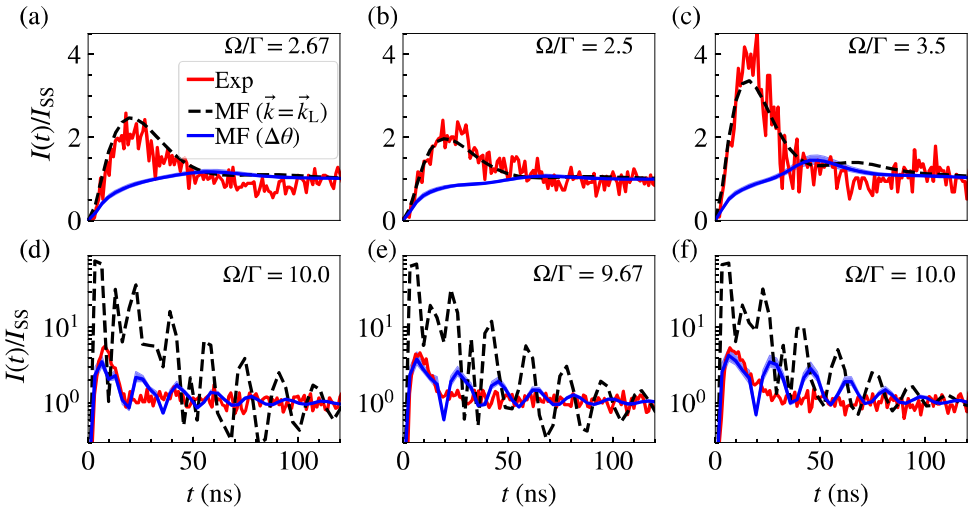

FIG. 13. The dynamics of the intensity for the MF dipolar model in the forward direction (dashed black line), averaged over a solid angle ($\Delta\theta=\theta_{out}-\theta_{in}$) about the forward direction with $\theta_{in}=\pi/22$ and $\theta_{out}=\pi/7\pm\pi/50$ (solid blue line, blue-shaded region), with experimental data (red traces) [83]. The intensity $I(t)$ has been scaled by its steady-state value, I_{SS}, for each data set. (a)–(c) The weak- and intermediate-driving regimes ($\Omega\le\Omega_C^{dipolar}$). (d)–(f) The strong-driving regime ($\Omega>\Omega_C^{dipolar}$). (a),(d) $N=1300$, $\Omega_C^{dipolar}\approx 2.9\Gamma$; (b),(e) $N=1500$, $\Omega_C^{dipolar}\approx 3.1\Gamma$; (c),(f) $N=1900$, $\Omega_C^{dipolar}\approx 3.5\Gamma$.

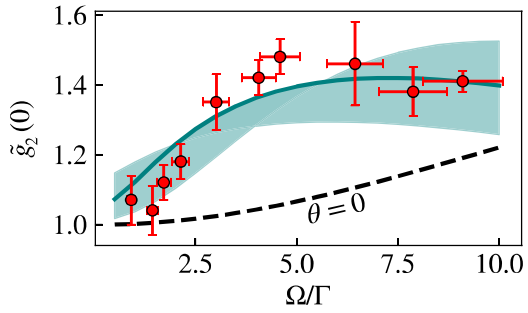

FIG. 14. $\tilde{g}_2(0)$ in the steady state for $N = 1400$: in the forward direction ($\theta = 0$, dashed black line), averaged over a solid angle ($\Delta\theta = \theta_{\text{out}} - \theta_{\text{in}}$) about the forward direction with $\theta_{\text{in}} = \pi/22$ and $\theta_{\text{out}} = \pi/16 \pm \pi/100$ (green-shaded region), with experimental data (red dots) from Ref. [61].

atomic cloud closer to the filter and the detector, changing the solid angle of the detected light. Of course, the radiative force may also lead to other motional effects such as dephasing, which we have not considered here.

In Fig. 14, we look at the steady-state equal-time two-point photon correlation function $\tilde{g}_2(0)$, as defined in Eq. (9), in the strictly forward direction ($\theta = 0$, dashed black line) and averaged over an annular region around the forward direction—the same as we did for the intensity earlier, with the same $\theta_{\text{in}} = \pi/22$ but with a smaller $\theta_{\text{out}} = \pi/16 \pm \pi/100$ (green-shaded region). Again, we find fair agreement between the experimental (red dots) [61] and numerical (green-shaded region) values, when averaged over the solid angle. We see some discrepancies at intermediate Ω/Γ values, which could arise from the dephasing of coherences due to atomic motion in the experiment. The best-fit θ_{out} values are not identical to the ones used for the intensity plots but such changes could occur between different experimental measurements. Here, we plot the numerical values for the noninteracting model instead of the dipolar model, as we find that it is quicker to integrate over the solid angle analytically over the steady state of the noninteracting model than to do a discrete sum in this case. We have already shown that the $\tilde{g}_2(0)$ values for the noninteracting model coincide with those of the MF dipolar model in Fig. 5(d), so we expect these values to be valid for our system. For further details about the analytical averaging of $\tilde{g}_2(0)$ for the noninteracting model, see Appendix A. We find that the solid angle for fitting the forward intensity and the $\tilde{g}_2(0)$ data has some variation across data sets. This is likely due to the uncertainties associated with the spatial filter in the current experimental data and hopefully our work will stimulate new measurements that can resolve and shed light on this disagreement in future research.

VI. CONCLUSIONS

We have studied the age-old, albeit complicated, problem of characterizing the emission properties of a spatially extended ensemble of driven interacting atoms in free space. What makes this problem complicated is the lack of symmetries such as translational invariance in periodic arrays and permutational invariance in optical cavities. In the absence of symmetries, an exact microscopic treatment of the system is impossible due to its exponentially large Hilbert space (approximately 2^N). Nevertheless, we are able to greatly reduce the complexity of the problem by identifying two distinct driving regimes (weak and strong), where an MF treatment is almost exact and the problem becomes at least numerically tractable with just $3N$ degrees of freedom. Furthermore, we find that our MF numerics are able to qualitatively capture the physics across all driving regimes and that beyond-MF methods (MACEMF and cumulant) lead to negligible corrections.

We find a crossover between nonequilibrium phases in the steady state of our system as a function of the driving strength Ω/Γ, akin to the superradiant phase transition in the CRF model. We find that the inhomogeneity of free-space dipolar interactions plays a key role in making our system strikingly different from the CRF model. This is most prominent in the N scaling of the critical order parameter, which is $\propto \sqrt{N}$ in our system and differs from that in the permutationally invariant CRF model ($\propto N$). Moreover, the strongly driven phase in our model is completely mixed and single-particle-like, whereas the "normal" phase of the CRF has collective quantum correlations.

At the cloud densities considered, our system is governed by the far-field dipolar interaction (approximately $1/r$), which is long range in quasi-1D. The collective effects of the long-range interactions are tempered by the dephasing arising from inhomogeneous frequency shifts and free-space emission. Using these physical insights, we propose a heuristic modified CRF model capable of describing our system, which includes single-particle dephasing, shearing, and spontaneous emission. This modified CRF is able to qualitatively reproduce the emergent features of our complicated microscopic dipolar model and is analytically solvable at the mean-field level.

While there has been considerable recent interest in this area with other works [53,54] looking into the light emission and critical properties of driven-dissipative atomic arrays, our work goes beyond the existing literature, which ignores the laser-induced spatial phase, and studies a system that is closer to the experimental implementation. The laser phase, for example, is key to enabling collective effects in our system. Not only is it responsible for canceling the phases in the Green's function along the forward direction but it also leads to a finite average frequency shift and a nontrivial scaling of the critical drive with respect to N. Previous work [53] characterizing the critical drive has not found a relevant N scaling. In addition, other works [53,54] have not looked carefully into the effects of strong disorder, which breaks translational invariance. For

our system, both disorder and laser phases play an important role in determining the dynamical behaviors. Disorder dephases the coherences and suppresses the N scaling of the critical drive from N (translationally invariant case) to $\sqrt{N}$. To the best of our knowledge, the N scaling presented here has not been reported before.

More importantly, our results are able to reproduce most of the experimental findings from a recent work [61]. Our work bridges the theoretical gap between the widely studied CRF model and the spatially extended inhomogeneous atomic ensembles accessible in current experimental setups. While previous work has shed some light on the properties of dilute atomic ensembles, our work extends this knowledge to moderately dense ensembles where collective effects are relevant beyond just frequency shifts and linewidth broadening.

For future work, it would be useful to measure (using Ramsey spectroscopy) the collective frequency shift arising from dipolar interactions, which leads to a nonzero $\langle\hat{\tilde{S}}_x\rangle$ in the dipolar model, as opposed to the CRF and noninteracting models, where $\langle\hat{\tilde{S}}_x\rangle = 0$. This is a smoking-gun signature of many-body effects in this system. The next step would be to study highly dense atomic ensembles, where the near-field elastic dipolar interactions (approximately $1/r^3$) dominate the physics and the MF treatment breaks down. The effects of atomic motion would become pertinent in the presence of strong light-matter interactions in dense ensembles. Another avenue worth exploring is the case of multilevel atoms, which includes the internal level structure of alkaline-earth(-like) atoms due to hyperfine splitting. Even in the weak-driving regime, the multilevel system can have quantum correlations in the ground-state manifold [84] and is distinct from the semiclassical two-level picture. While there has been some recent work on the emission properties of multilevel arrays in free space, it is largely confined to the early-time dynamics [85] and inverted arrays [50]. Characterizing the steady-state properties of multilevel ensembles is crucial for current experiments and remains an unsolved problem.

Note added.—During the completion of our work, we became aware of a related recent work [82] that reaches conclusions similar to ours using a complementary theoretical treatment.

ACKNOWLEDGMENTS

We thank Jarrod T. Reilly, Eric Yilun Song, and James K. Thompson for insightful discussions and feedback on our manuscript. We wish to acknowledge support by the Vannevar Bush Faculty Fellowship (VBFF), the Air Force Office of Scientific Research (AFOSR) via Grant No. FA9550-24-1-0179, by the National Science Foundation (NSF) JILA Physics Frontier Center (PFC) via Grants No. PHY-2317149 and No. QLCI-OMA-2016244, by the U.S. Department of Energy, Office of Science, National Quantum Information Science Research Centers Quantum Systems Accelerator, and by NIST.

APPENDIX A: NONINTERACTING MODEL

Here, we consider the noninteracting system and its steady-state solution. The master equation describing this system is $\dot{\hat{\rho}} = -i[\hat{H}_0, \hat{\rho}] + \mathcal{L}_0(\hat{\rho})$, where $\hat{H}_0 = -(\Omega/2)\sum_k (e^{i\vec{k}_L\cdot\vec{r}_k}\hat{\sigma}_k^+ + \text{h.c.})$ is the Hamiltonian and $\mathcal{L}_0(\hat{\rho}) = (\Gamma/2)\sum_j \left(2\hat{\sigma}_j^-\hat{\rho}\hat{\sigma}_j^+ - \{\hat{\sigma}_j^z, \hat{\rho}\}/2 - \hat{\rho}\right)$ is the Lindbladian. The atomic equations of motion reduce to the standard optical Bloch equations:

$$\langle\dot{\hat{\sigma}}_k^z\rangle = -\Gamma\left(\langle\hat{\sigma}_k^z\rangle + 1\right) + i\Omega\left(e^{i\vec{k}_L\cdot\vec{r}_k}\langle\hat{\sigma}_k^+\rangle - e^{-i\vec{k}_L\cdot\vec{r}_k}\langle\hat{\sigma}_k^-\rangle\right), \tag{A1}$$

$$\langle\dot{\hat{\sigma}}_k^+\rangle = -\frac{\Gamma}{2}\langle\hat{\sigma}_k^+\rangle + i\frac{\Omega}{2}e^{-i\vec{k}_L\cdot\vec{r}_k}\langle\hat{\sigma}_k^z\rangle, \tag{A2}$$

and the steady state can be obtained by setting $\langle\dot{\hat{\sigma}}_k^z\rangle = 0$ and $\langle\dot{\hat{\sigma}}_k^+\rangle = 0$ for all k, as

$$\langle\hat{\sigma}_k^z\rangle = -\frac{\Gamma^2}{\Gamma^2 + 2\Omega^2} \equiv -R, \tag{A3}$$

$$\langle\hat{\sigma}_k^+\rangle = -i\frac{\Omega}{\Gamma}e^{-i\vec{k}_L\cdot\vec{r}_k}R. \tag{A4}$$

The steady-state intensity in an observed direction $\vec{k}$ is

$$\begin{aligned}\frac{I(\vec{k})}{I_0(\vec{k})} &= \sum_j\left(\frac{\langle\hat{\sigma}_j^z\rangle + 1}{2}\right) + \sum_{i\neq j}\langle\hat{\sigma}_i^+\rangle\langle\hat{\sigma}_j^-\rangle e^{i\vec{k}\cdot(\vec{r}_i - \vec{r}_j)} \\ &= \frac{(1-R)}{2}N + \frac{\Omega^2}{\Gamma^2}R^2\sum_{i\neq j}e^{i(\vec{k}-\vec{k}_L)\cdot(\vec{r}_i-\vec{r}_j)}.\end{aligned} \tag{A5}$$

The two-photon correlation function in an observed direction $\vec{k}$ is

$$\tilde{g}_2(0)(\vec{k}) = \frac{\langle\hat{\tilde{S}}^+(\vec{k})\hat{\tilde{S}}^+(\vec{k})\hat{\tilde{S}}^-(\vec{k})\hat{\tilde{S}}^-(\vec{k})\rangle}{\langle\hat{\tilde{S}}^+(\vec{k})\hat{\tilde{S}}^-(\vec{k})\rangle^2}, \tag{A6}$$

where $\hat{\tilde{S}}_\pm(\vec{k}) = \sum_i \hat{\sigma}_i^\pm e^{\pm i\vec{k}\cdot\vec{r}_i}$. For noninteracting particles, the correlations factor for different atoms as $\langle\hat{\sigma}_\alpha^i\hat{\sigma}_\beta^j\rangle = \langle\hat{\sigma}_\alpha^i\rangle\langle\hat{\sigma}_\beta^j\rangle$. For the same atom, we use the commutation relations of the Pauli operators as $\langle\hat{\sigma}_\alpha^i\hat{\sigma}_\beta^i\rangle = \delta_{\alpha,\beta}\mathbb{1} + 2i\varepsilon^{\alpha\beta\gamma}\langle\hat{\sigma}_\gamma^i\rangle$, where $\alpha,\beta,\gamma \in \{x,y,z\}$. Using this scheme, the two-photon correlation function along the measurement direction can be expressed as

$$\tilde{g}_2(0)(\vec{k}_\mathrm{L}) = \left(\frac{1}{2}\sum_{\langle ij\rangle}\left(\langle\hat{\sigma}_i^z\rangle+1\right)\left(\langle\hat{\sigma}_j^z\rangle+1\right)+2\sum_{\langle ijk\rangle}\left(\langle\hat{\sigma}_i^z\rangle+1\right)\langle\hat{\tilde{\sigma}}_j^+\rangle\langle\hat{\tilde{\sigma}}_k^-\rangle+\sum_{\langle ijkl\rangle}\langle\hat{\tilde{\sigma}}_i^+\rangle\langle\hat{\tilde{\sigma}}_j^+\rangle\langle\hat{\tilde{\sigma}}_k^-\rangle\langle\hat{\tilde{\sigma}}_l^-\rangle\right)$$
$$\times\left(\frac{1}{2}\sum_i\left(\langle\hat{\sigma}_i^z\rangle+1\right)+\sum_{\langle ij\rangle}\langle\hat{\tilde{\sigma}}_i^+\rangle\langle\hat{\tilde{\sigma}}_j^-\rangle\right)^{-2}, \tag{A7}$$

where we have suppressed the notation to denote $\hat{\tilde{\sigma}}_j^+ \equiv \hat{\sigma}_j^+ e^{i\vec{k}_\mathrm{L}\cdot\vec{r}_j}$ and $\langle ij\ldots\rangle$ denotes sum over unlike indices, i.e., $i\neq j\neq\ldots$.

1. Weak-driving regime

In the weak-driving regime ($\Omega \ll \Gamma$), the steady-state solution can be expressed as

$$\langle\hat{\sigma}_k^z\rangle = -\left(1-\frac{2\Omega^2}{\Gamma^2}\right) \tag{A8}$$

$$\langle\hat{\sigma}_k^+\rangle = i\frac{\Omega}{\Gamma}e^{-i\vec{k}_\mathrm{L}\cdot\vec{r}_k} \tag{A9}$$

and the intensity along the laser wave vector is

$$\frac{I(\vec{k}_\mathrm{L})}{I_0(\vec{k}_\mathrm{L})} = \frac{\Omega^2}{\Gamma^2}N\left(N-\frac{1}{2}\right)\approx\frac{\Omega^2}{\Gamma^2}N^2, \tag{A10}$$

which scales as N^2 in the large-N limit due to the constructive interference of coherences along the measurement direction. In this regime, the two-photon correlation function can be expressed as

$$\tilde{g}_2(0)(\vec{k}_\mathrm{L}) = 1-\frac{2}{N}+\frac{1}{N^2}\Rightarrow\lim_{N\to\infty}\tilde{g}_2(0)(\vec{k}_\mathrm{L})=1, \tag{A11}$$

which is consistent with the value for a coherent state. In the extreme weak-driving limit, the atoms are very weakly excited such that $\langle\hat{\sigma}_j^z\rangle\to-1$, which, along with Eq. (A7), gives $\tilde{g}_2(0)(\vec{k}_\mathrm{L})\to 1$.

2. Strong-driving regime

In the strong-driving regime ($\Omega \gg \Gamma$), the steady-state solution can be expressed as

$$\langle\hat{\sigma}_k^z\rangle = -\frac{\Gamma^2}{2\Omega^2} \tag{A12}$$

$$\langle\hat{\sigma}_k^+\rangle = i\frac{\Gamma}{2\Omega}e^{-i\vec{k}_\mathrm{L}\cdot\vec{r}_k} \tag{A13}$$

and the intensity along the laser wave vector is given by

$$\frac{I(\vec{k}_\mathrm{L})}{I_0(\vec{k}_\mathrm{L})} = \frac{N}{2}+\frac{\Gamma^2}{4\Omega^2}N(N-2). \tag{A14}$$

When the drive is in the regime $\Gamma^2/4\Omega^2 < 1/N \Rightarrow \Omega > \Gamma\sqrt{N}/2$ for all N, the intensity scales as N. As the drive gets extremely large, $\Omega \gg N\Gamma/2$, the state gets fully mixed and $I(\vec{k}_\mathrm{L})\to N/2$. In this limit, we obtain

$$\tilde{g}_2(0) = 2-\frac{2}{N}\Rightarrow\lim_{N\to\infty}\tilde{g}_2(0)=2, \tag{A15}$$

consistent with the fact that the system is described by a thermal state. In the extreme strong-driving limit, the system is maximally mixed such that $\langle\hat{\sigma}_j^z\rangle\to 0$ and $\langle\hat{\sigma}_j^{+,-}\rangle\to 0$. Plugging this into Eq. (A7) also gives $\tilde{g}_2(0)(\vec{k}_\mathrm{L})\to 2$.

3. Averaging over a solid angle

For our pencil-shaped cloud (Fig. 2), the atomic positions are distributed in a Gaussian distribution,

$$\rho(x,y,z) = \frac{N\exp\left(-\frac{x^2}{2\sigma_\mathrm{ax}^2}-\frac{y^2+z^2}{2\sigma_\mathrm{rad}^2}\right)}{(2\pi)^{3/2}\sigma_\mathrm{ax}\sigma_\mathrm{rad}^2}, \tag{A16}$$

where $\sigma_\mathrm{ax}=20\lambda$ and $\sigma_\mathrm{rad}=\lambda/2$ are the axial and radial standard deviations of the cloud, respectively. Then, in the large-N limit, we can replace the sum over atoms i and j in the intensity in Eq. (A5) by an integral over the positions, weighted by their distribution $\rho(x,y,z)$, as

$$\frac{I(\vec{k})}{I_0(\vec{k})}\approx\frac{(1-R)}{2}N-\frac{\Omega^2}{\Gamma^2}R^2N + \frac{\Omega^2}{\Gamma^2}R^2\int d^3r\int d^3r'\rho(\vec{r})\rho(\vec{r}')e^{i(\vec{k}-\vec{k}_\mathrm{L})\cdot(\vec{r}-\vec{r}')}, \tag{A17}$$

where in the first line we have subtracted the contribution from the $i=j$ term in the integral. We define $\vec{q}=\vec{k}-\vec{k}_{\rm L}=(q_x,q_y,q_z)$. Then, it is easy to do obtain the integral in Cartesian coordinates as

$$\begin{aligned} A &= \left|\int_{-\infty}^{\infty}dx\int_{-\infty}^{\infty}dy\int_{-\infty}^{\infty}dz\,\rho(x,y,z)e^{i(q_x x+q_y y+q_z z)}\right|^2 \\ &= N^2\exp(-(\sigma_{\rm ax}^2q_x^2+\sigma_{\rm rad}^2q_y^2+\sigma_{\rm rad}^2q_z^2)). \end{aligned} \tag{A18}$$

Now, we substitute $\vec{k}_{\rm L}=(2\pi/\lambda)\hat{x}$ and $\vec{k}=(2\pi/\lambda)\ (\cos\theta,\sin\theta\cos\phi,\sin\theta\sin\phi)$, where θ is the angle from the $\hat{x}$ axis (forward direction) and ϕ is the azimuthal angle in the y-z plane from $\hat{y}$. Then, we obtain the intensity as

$$\frac{I(\theta,\phi)}{I_0(\vec{k})}=\frac{2(\Omega/\Gamma)^4}{(1+2(\Omega/\Gamma)^2)^2}N\left[1+\frac{N\exp(-(2\pi)^2(\sigma_{\rm ax}^2(1-\cos\theta)^2+\sigma_{\rm rad}^2\sin^2\theta))}{2(\Omega/\Gamma)^2}\right]. \tag{A19}$$

Close to the forward direction $\theta\equiv\delta\theta\approx 0$, the intensity can be expressed as

$$\frac{I(\delta\theta,\phi)}{I_0(\vec{k})}\approx\frac{2(\Omega/\Gamma)^4}{(1+2(\Omega/\Gamma)^2)^2}N\left[1+\frac{Ne^{-(2\pi)^2(\sigma_{\rm rad}^2\delta\theta^2+\sigma_{\rm ax}^2\delta\theta^4/4)}}{2(\Omega/\Gamma)^2}\right], \tag{A20}$$

such that the N^2 enhancement falls off exponentially fast as the observation direction deviates from the forward direction.

We need to multiply the above intensity equation [Eq. (A19)] by the geometric factor $I_0(\hat{k})$. Due to the large distance of the detector from the cloud, $I_0(\hat{k})$ is the factor associated with the far-field part of the electromagnetic Green's tensor and appears in the expression of the dipolar intensity pattern as $I_0(\hat{k})=\hat{e}_q\cdot(\mathbb{1}-\hat{k}\otimes\hat{k})\cdot(\mathbb{1}-\hat{k}\otimes\hat{k})\cdot\hat{e}_q^*$, where $\hat{e}_q$ is the polarization of light associated with the atomic transition corresponding to fluorescence. For circularly polarized light, we obtain $I_0(\hat{k})=(1+\sin^2\theta\sin^2\phi)/2$.

Then, the intensity can be averaged over an annular region, which has $\theta_{\rm in}=\pi/22$ and $\theta_{\rm out}=\pi/7$ as the inner and outer boundaries, to obtain

$$\begin{aligned} \langle I\rangle &\equiv \int_0^{2\pi}d\phi\int_{\theta_{\rm in}}^{\theta_{\rm out}}d\theta I(\theta,\phi)\sin\theta(1+\sin^2\theta\sin^2\phi)/(2A) \\ &\approx [2(\Omega/\Gamma)^4/(1+2(\Omega/\Gamma)^2)^2]N\left\{c_A^{\rm I}\right. \\ &\quad \left.+[c_A^{\rm II}N/2(\Omega/\Gamma)^2]\right\}, \end{aligned}$$

where $A=\int_0^{2\pi}d\phi\int_{\theta_{\rm in}}^{\theta_{\rm out}}d\theta\sin\theta$. It can be seen that the extra factor of $c_A^{\rm II}/c_A^{\rm I}\approx 0.022$, due to the averaging over a finite solid angle around the forward direction, reduces the relative strength of the coherent emission and shifts the peak of the intensity to lower Ω/Γ. We have substituted $\sigma_{\rm ax}=\lambda/2$ and $\sigma_{\rm rad}=20\lambda$ above, corresponding to our system (Fig. 2), to obtain a numerical value.

Similarly, we can also integrate over the atomic positions, weighted by the Gaussian distribution, to obtain the analytical expression for the steady-state two-photon correlation function, $\tilde{g}_2(\vec{k},\vec{k}')$, defined in Eq. (9), in terms of $\hat{k}\equiv(\theta,\phi)$ and $\hat{k}'\equiv(\theta',\phi')$.

APPENDIX B: MEAN-FIELD DIPOLAR MODEL

The mean-field equations of motion for the dipolar model can be obtained from the master equation by factoring the multi-atom correlations as $\langle\hat{A}_k\hat{B}_j\rangle=\langle\hat{A}_k\rangle\langle\hat{B}_j\rangle$, where $j\neq k$. For an atom k, this treatment leads to

$$\begin{aligned} \langle\dot{\hat{\sigma}}_k^z\rangle &= -\Gamma\left(\langle\hat{\sigma}_k^z\rangle+1\right)+2i\left(\frac{\Omega}{2}e^{i\vec{k}_L\cdot\vec{r}_k}+\sum_{\substack{j=1\\j\neq k}}^{N}\mathcal{G}_{kj}\langle\hat{\sigma}_j^-\rangle\right)\langle\hat{\sigma}_k^+\rangle \\ &\quad -2i\left(\frac{\Omega}{2}e^{-i\vec{k}_L\cdot\vec{r}_k}+\sum_{\substack{j=1\\j\neq k}}^{N}\mathcal{G}_{kj}^*\langle\hat{\sigma}_j^+\rangle\right)\langle\hat{\sigma}_k^-\rangle, \end{aligned} \tag{B1}$$

$$\langle\dot{\hat{\sigma}}_k^+\rangle=-\frac{\Gamma}{2}\langle\hat{\sigma}_k^+\rangle+i\left(\frac{\Omega}{2}e^{-i\vec{k}_L\cdot\vec{r}_k}+\sum_{\substack{j=1\\j\neq k}}^{N}\mathcal{G}_{kj}^*\langle\hat{\sigma}_j^+\rangle\right)\langle\hat{\sigma}_k^z\rangle, \tag{B2}$$

where $\mathcal{G}_{kj}=\mathcal{R}_{kj}+i\mathcal{I}_{kj}=\mathcal{G}_{jk}$ is the dipolar interaction coefficient and is symmetric with respect to the indices. We can see from the above equations that the dipolar-interaction term acts like an effective time-dependent complex drive with a strength that depends on the coherence of other atoms in the array. The elastic and inelastic dipolar

coefficients are the real and imaginary parts, respectively, of the free-space electromagnetic Green's function,

$$\mathcal{R}_{kj} = (3\Gamma/4)\left[(1-\cos^2\theta)\frac{\cos(k_0 r)}{k_0 r} + (1-3\cos^2\theta)\left(-\frac{\sin(k_0 r)}{(k_0 r)^2} - \frac{\cos(k_0 r)}{(k_0 r)^3}\right)\right],$$
$$\mathcal{I}_{kj} = (3\Gamma/4)\left[(1-\cos^2\theta)\frac{\sin(k_0 r)}{k_0 r} + (1-3\cos^2\theta)\left(\frac{\cos(k_0 r)}{(k_0 r)^2} - \frac{\sin(k_0 r)}{(k_0 r)^3}\right)\right],$$

where $r = |\vec{r}_{kj}|$, $\cos\theta = \hat{r}_{kj}\cdot\hat{e}_q$, $q = 0, \pm 1$, θ is the angle between the polarization of the atomic transition ($\hat{e}_q$, orientation of the transition "dipole") and the inter-atomic distance. For the MF dipolar model at the densities considered in this paper, $k_0\bar{r} \geq 1$ and the physics is dominated by the $1/r$ (far-field) term, where $\bar{r}$ is the average inter-atomic distance. The far-field interaction coefficients are somewhat simpler,

$$\mathcal{R}_{kj} \approx (3\Gamma/4)(1-\cos^2\theta)\frac{\cos(k_0 r)}{k_0 r},$$
$$\mathcal{I}_{kj} \approx (3\Gamma/4)(1-\cos^2\theta)\frac{\sin(k_0 r)}{k_0 r},$$

and we have $\mathcal{G}_{kj} = \mathcal{R}_{kj} + i\mathcal{I}_{kj} \approx (3\Gamma/4)(1-\cos^2\theta)e^{ik_0 r}/(k_0 r)$. By gauging away the phase of the laser, we can rewrite the MF equations as

$$\langle\dot{\hat{\sigma}}_k^z\rangle = -\Gamma\left(\langle\hat{\sigma}_k^z\rangle + 1\right) + 2i\left(\frac{\Omega}{2} + \sum_{\substack{j=1\\ j\neq k}}^{N}\tilde{\mathcal{G}}_{kj}\langle\hat{\tilde{\sigma}}_j^-\rangle\right)\langle\hat{\tilde{\sigma}}_k^+\rangle$$
$$- 2i\left(\frac{\Omega}{2} + \sum_{\substack{j=1\\ j\neq k}}^{N}\tilde{\mathcal{G}}_{kj}^*\langle\hat{\tilde{\sigma}}_j^+\rangle\right)\langle\hat{\tilde{\sigma}}_k^-\rangle, \tag{B3}$$

$$\langle\dot{\hat{\tilde{\sigma}}}_k^+\rangle = -\frac{\Gamma}{2}\langle\hat{\tilde{\sigma}}_k^+\rangle + i\left(\frac{\Omega}{2} + \sum_{\substack{j=1\\ j\neq k}}^{N}\tilde{\mathcal{G}}_{kj}^*\langle\hat{\tilde{\sigma}}_j^+\rangle\right)\langle\hat{\sigma}_k^z\rangle, \tag{B4}$$

where we have included the laser phase in the interaction coefficient as $\tilde{\mathcal{G}}_{kj} = \mathcal{G}_{kj}e^{-i\vec{k}_L\cdot\vec{r}_{kj}} \approx (3\Gamma/4)(1-\cos^2\theta)e^{i(k_0 r - \vec{k}_L\cdot\vec{r}_{kj})}/(k_0 r)$, in the far-field limit. This additional phase leads to constructive interference of interaction terms in the direction of the laser wave vector, i.e., $k_0 r - \vec{k}_L\cdot\vec{r}_{kj} = 0$. For our setup, $\vec{k}_L = 2\pi/\lambda\hat{x} \Rightarrow \vec{k}_L\cdot\vec{r}_{kj} = k_0(x_k - x_j)$ and in the quasi-1D gas, we have $|\vec{r}_{kj}| \approx |x_k - x_j|$ and $\cos^2\theta \approx |\hat{x}\cdot\hat{e}_q|^2$ ($q = 0, \pm 1$) for the majority of atomic pairs. For a linearly polarized atomic transition ($\hat{e}_0 = \hat{z}$), $|\hat{x}\cdot\hat{e}_q|^2 = 0$ and for a circularly polarized transition ($\hat{e}_+ = -(\hat{x} + i\hat{y})/\sqrt{2}$), $|\hat{x}\cdot\hat{e}_q|^2 = 1/2$. Then, $\tilde{\mathcal{G}}_{k>j,j} \approx (3\Gamma/8)/(k_0 r)$ and $\tilde{\mathcal{G}}_{k<j,j} \approx (3\Gamma/8)e^{2ik_0 r}/(k_0 r)$, where we have assumed that the atomic indices are sorted in increasing order of position along the x axis. Unlike in periodic arrays with special lattice spacing such that $e^{2ik_0 r} = 1$, in a disordered array the $e^{2ik_0 r}$ phases in $\tilde{\mathcal{G}}_{k<j,j}$ terms would get washed out in comparison to the $\tilde{\mathcal{G}}_{k>j,j}$ terms. In the MF equations of motion, we have constructive interference of terms approximately $\tilde{\mathcal{G}}_{k>j,j}\langle\hat{\tilde{\sigma}}_j^-\rangle\langle\hat{\tilde{\sigma}}_k^+\rangle$. This implies that due to the phase matching of dipolar interactions with the laser drive, effects will constructively add up from an atom k further along in the path of the laser absorbing a photon emitted from an atom j earlier in the path of the laser.

1. N scaling of intensity

Here, we discuss how the forward intensity scales with N at a fixed value of $\Omega/\Omega_C^{\text{dipolar}}$, which fixes the regime (weak or strong driving) of the system. We define the N scaling as $\langle\hat{\tilde{S}}_+\hat{\tilde{S}}_-\rangle \propto N^{\alpha(\Omega/\Omega_C^{\text{dipolar}},N)}$, the same as in the main text, such that $\alpha(\Omega/\Omega_C^{\text{dipolar}},N)$ varies slowly with N. We show this slow variation with N in Fig. 15 (right), where the power-law scaling, $\alpha(\Omega/\Omega_C^{\text{dipolar}},N)$, is calculated between black dots, which correspond to the upper limits of the N values for the fits and the lower limit for each fit is approximately $0.6N$. Corresponding to these fits, we show the power-law scaling, $\alpha(\Omega/\Omega_C^{\text{dipolar}},N)$, in Fig. 15 (left), which remains almost constant with N in the strong-driving regime $\Omega/\Omega_C^{\text{dipolar}} > 1$, where the

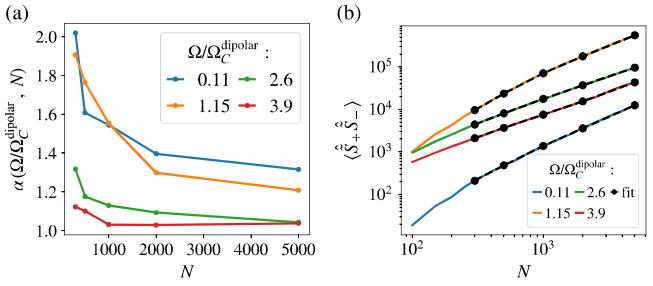

FIG. 15. (a) The N dependence of the N scaling of the forward intensity, $\langle\hat{\tilde{S}}_+\hat{\tilde{S}}_-\rangle \propto N^{\alpha(\Omega/\Omega_C^{\text{dipolar}},N)}$. (b) The MF steady-state intensity (solid line) versus N and best fits (dotted-dashed black line) of the intensity to a power law in N corresponding to the $\alpha(\Omega/\Omega_C^{\text{dipolar}},N)$ values on the left.

system becomes mixed and we get the single-particle-like linear scaling with N. In the weak-driving regime, $\Omega/\Omega_C^{\text{dipolar}} < 1$, we see that $\alpha(\Omega/\Omega_C^{\text{dipolar}}, N) \sim 2$ at small N, where almost perfect phase-matching occurs in the dilute limit. As N increases, the system gets denser and interaction-induced shifts lead to dephasing, reducing $\alpha(\Omega/\Omega_C^{\text{dipolar}}, N)$. Thus, at fixed $\Omega/\Omega_C^{\text{dipolar}}$, as N is increased, the physics changes from the dilute to the strongly interacting regime, which is reflected in the value of $\alpha(\Omega/\Omega_C^{\text{dipolar}}, N)$.

APPENDIX C: CRF MODEL ANALYSIS

Consider the CRF master equation given by

$$\frac{\partial\hat{\rho}}{\partial t} = -i\Omega\left[\hat{S}_x, \hat{\rho}\right] + \Gamma\left(\hat{S}_-\hat{\rho}\hat{S}_+ - \frac{1}{2}\{\hat{S}_+\hat{S}_-, \hat{\rho}\}\right). \quad \text{(C1)}$$

Equation (C1) can be rewritten in the following form:

$$\frac{\partial\hat{\rho}}{\partial t} = \Gamma\left(\hat{O}\hat{\rho}\hat{O}^\dagger - \frac{1}{2}\{\hat{O}^\dagger\hat{O}, \hat{\rho}\}\right), \quad \text{(C2)}$$

where

$$\hat{O} = \hat{S}_- + i\beta\frac{N}{2} = \hat{S}_x - i\hat{S}_y + i\beta\frac{N}{2}, \quad \text{(C3)}$$

where β is the order parameter and is given by $\beta = \Omega/\Omega_c$ with $\Omega_c = N\Gamma/2$. From the factorization of Eq. (C2), we can infer the properties of the steady state [86].

For $\beta < 1$, the system is in the superradiant phase. To analyze the stable state within the polarized phase, we employ a Holstein-Primakoff expansion centered around the polarization direction. In mean-field theory, the Bloch vector stabilizes at an angle θ, where $\sin\theta = \beta$. This leads us to consider a rotated coordinate system:

$$\hat{S}_x = \hat{S}'_x, \quad \text{(C4)}$$

$$\hat{S}_y = \hat{S}'_y\cos\theta - \hat{S}'_z\sin\theta, \quad \text{(C5)}$$

$$\hat{S}_z = \hat{S}'_z\cos\theta + \hat{S}'_y\sin\theta, \quad \text{(C6)}$$

such that the Bloch vector is aligned along $-z'$. We then do a Holstein-Primakoff (HP) expansion about this direction, with the (lowest-order) replacements $\hat{S}'_z \approx -(N/2)$, $\hat{S}'_x \approx \hat{x}\sqrt{N/2}$, and $\hat{S}'_y \approx -\hat{p}\sqrt{N/2}$, with $\hat{x} = (\hat{a} + \hat{a}^\dagger)/\sqrt{2}$ and $\hat{p} = (\hat{a} - \hat{a}^\dagger)/\sqrt{2}i$, which satisfies $\left[\hat{x}, \hat{p}\right] = i$. The operator $\hat{O}$ in Eq. (C3) in the HP expansion will have the form

$$\hat{O} = \hat{S}_x - i\hat{S}_y + i\beta\frac{N}{2} \approx \sqrt{\frac{N}{2}}\left(\hat{x} + i\hat{p}\cos\theta\right). \quad \text{(C7)}$$

For $\beta < 1$, the state is in the superradiant phase and will remain coherent. This implies that the density matrix of the steady state satisfies $\hat{\rho} = |0_D\rangle\langle 0_D|$ and $\hat{O}|0_D\rangle = 0$, i.e., $\hat{O}$ corresponds to an annihilation operator with unique dark state $|0_D\rangle$. To normalize properly $\hat{O}$, we recall that the annihilation operator $\hat{a}_D = m\hat{O}$ satisfies the commutation relation $\left[\hat{a}_D, \hat{a}_D^\dagger\right] = 1$. Replacing, we find that $m^2\left[\hat{x} + i\hat{p}\cos\theta, \hat{x} - i\hat{p}\cos\theta\right] = m^2\cos\theta\left(-2i^2\right) = 2m^2\cos\theta = 1$, so $m = 1/\sqrt{2\cos\theta}$ and the annihilation operator reads as $\hat{a}_D = \left(\hat{x} + i\hat{p}\cos\theta\right)/\sqrt{2\cos\theta}$. In these terms, we can define $\hat{x}_D = (\hat{a}_D + \hat{a}_D^\dagger)/\sqrt{2}$ and $\hat{p}_D = (\hat{a}_D - \hat{a}_D^\dagger)/\sqrt{2}i$, so we can find that $\hat{x} = \sqrt{\cos\theta}\hat{x}_D$ and $\hat{p} = \hat{p}_D/\sqrt{\cos\theta}$. These operators will allow us to calculate expected values in the superradiant regime.

Our aim is to find expressions that represent the behavior of the expected values of the operators of interest at the limit of a large number of particles. Replacing the operators of Eq. (C6) expanded in HP, we find that

$$\hat{S}_x \approx \hat{x}_D\sqrt{\frac{N}{2}\cos\theta}, \quad \text{(C8)}$$

$$\hat{S}_y \approx \frac{N}{2}\sin\theta - \hat{p}_D\sqrt{\frac{N}{2}\cos\theta}, \quad \text{(C9)}$$

$$\hat{S}_z \approx -\frac{N}{2}\cos\theta - \hat{p}_D\sqrt{\frac{N}{2\cos\theta}}\sin\theta. \quad \text{(C10)}$$

From the mean-field analysis, we can obtain that $\left\langle\hat{S}_x\right\rangle = 0$, $\left\langle\hat{S}_y\right\rangle = N/2\sin\theta$ and $\left\langle\hat{S}_z\right\rangle = -N/2\cos\theta$ [86]. For the expected value $\left\langle\hat{S}_+\hat{S}_-\right\rangle$ we can calculate using the HP expansion:

$$\begin{aligned}\hat{S}_+ = \hat{S}_x + i\hat{S}_y &\approx \hat{x}_D\sqrt{\frac{N}{2}\cos\theta} \\ &\quad + i\left(\frac{N}{2}\sin\theta - \hat{p}_D\sqrt{\frac{N}{2}\cos\theta}\right) \\ &= i\frac{N}{2}\sin\theta + \sqrt{\frac{N}{2}\cos\theta}\left(\hat{x}_D - i\hat{p}_D\right) \\ &= i\frac{N}{2}\sin\theta + \sqrt{N\cos\theta}\hat{a}_D^\dagger. \end{aligned} \quad \text{(C11)}$$

So, $\hat{S}_+\hat{S}_-$ expanded as a function of the HP operators and its expected value is

$$\begin{aligned}\hat{S}_+\hat{S}_- \approx &\left(i\frac{N}{2}\sin\theta + \sqrt{N\cos\theta}\hat{a}_D^\dagger\right) \\ &\times\left(-i\frac{N}{2}\sin\theta + \sqrt{N\cos\theta}\hat{a}_D\right),\end{aligned}$$

$$\left\langle \hat{S}_+\hat{S}_-\right\rangle = \left\langle 0_D\left|\hat{S}_+\hat{S}_-\right|0_D\right\rangle \approx i\frac{N}{2}\sin\theta\left(-i\frac{N}{2}\sin\theta\right) = \left(\frac{N}{2}\sin\theta\right)^2. \tag{C12}$$

We have used the fact that $\left\langle \hat{a}_D^\dagger\right\rangle = \langle \hat{a}_D\rangle = \left\langle \hat{a}_D^\dagger\hat{a}_D\right\rangle = 0$. This formula is valid for $\theta < \pi/2$, where the HP approximation holds.

Now, we estimate the expected value $\left\langle \hat{S}_+\hat{S}_+\hat{S}_-\hat{S}_-\right\rangle$ as

$$\left\langle \hat{S}_+\hat{S}_+\hat{S}_-\hat{S}_-\right\rangle = \left\langle 0_D\left|\hat{S}_+\hat{S}_+\hat{S}_-\hat{S}_-\right|0_D\right\rangle,$$
$$\hat{S}_-\left|0_D\right\rangle \approx -i\frac{N}{2}\sin\theta\left|0_D\right\rangle,$$
$$\left\langle \hat{S}_+\hat{S}_+\hat{S}_-\hat{S}_-\right\rangle \approx \left(i\frac{N}{2}\sin\theta\right)\left(-i\frac{N}{2}\sin\theta\right)\left\langle 0_D\left|\hat{S}_+\hat{S}_-\right|0_D\right\rangle = \left(\frac{N}{2}\sin\theta\right)^4. \tag{C13}$$

In this case, we find that $g_2(0) = \left\langle \hat{S}_+\hat{S}_+\hat{S}_-\hat{S}_-\right\rangle / \left\langle \hat{S}_+\hat{S}_-\right\rangle^2$ at the HP limit is $g_2(0) \approx (N/2\sin\theta)^4/\left((N/2\sin\theta)^2\right)^2 = 1$ for the superradiant phase. Regarding the HP approximation, this tends to improve at the limit of large numbers of particles such that it converges to the exact result [86], so we can expect that for $\beta < 1$ the previous result is valid at $N \to \infty$ and that, in these conditions, $g_2(0) = 1$.

For $\beta > 1$, we are in the normal phase. In that case, the steady state is highly mixed. In general, the steady state can be written formally as

$$\hat{\rho}_{\rm ss} = \mathcal{N}\frac{1}{\frac{\hat{S}_-}{N/2} + i\beta}\frac{1}{\frac{\hat{S}_+}{N/2} - i\beta}, \tag{C14}$$

where N is a normalization constant and $\beta = 2\Omega/(\Gamma N)$. In the normal phase ($\beta > 1$), the properties of the steady state are derived through semiclassical analysis. We parametrize the phase space using angles θ and ϕ as follows: $\left(\hat{S}_x, \hat{S}_y, \hat{S}_z\right) \to N/2\,(\sin\theta\cos\phi, \sin\theta\sin\phi, \cos\theta)$, so $\hat{S}_+ \to N/2\sin\theta e^{i\phi}$, and operator traces are replaced by integrals over the sphere, with the measure $N/4\pi\,\sin\theta\,d\theta\,d\phi$. The normalization constant N is determined through this process. To obtain $\mathcal{N}$, we recall the normalization condition $\mathrm{Tr}\left(\hat{\rho}_{\rm ss}\right) = 1$, so we need to satisfy

$$1 = \mathcal{N}\int_0^\pi\int_0^{2\pi}\frac{1}{\left(\sin\theta e^{-i\phi} + i\beta\right)\left(\sin\theta e^{i\phi} - i\beta\right)}\frac{N}{4\pi}\sin\theta d\phi d\theta. \tag{C15}$$

This integral can be done using calculus of residues around the unit circle $z = e^{i\phi}$ in the counterclockwise direction and we must be aware that $\sin\theta/\beta < 1$ in the normal phase, which will be relevant for determining the suitable residues inside the integration curve. In particular, the use of this substitution in Eq. (C15) leads to

$$1 = -\mathcal{N}\frac{N}{4\pi\beta}\int_0^\pi\left(\oint_{|z|=1}\frac{dz}{\left(z - i\frac{\sin\theta}{\beta}\right)\left(z - i\frac{\beta}{\sin\theta}\right)}\right)d\theta. \tag{C16}$$

In Eq. (C16) we can identify that the residue $z_{\rm res,1} = i(\sin\theta/\beta)$ belongs to the interior of the integration curve, whereas $z_{\rm res,2} = i(\beta/\sin\theta)$ does not belong because, for all θ, we have $\sin\theta < \beta$ in the normal phase. By the Cauchy integral formula, we deduce that

$$1 = \mathcal{N}\frac{N}{2}\int_0^\pi\frac{\sin\theta}{\beta^2 - \sin^2\theta}d\theta. \tag{C17}$$

From here, we find that $\mathcal{N} = \sqrt{\beta^2-1}/N\arctan\left(\left(\sqrt{\beta^2-1}\right)^{-1}\right)$.

The estimation of the expected values can be performed using a similar integration process such that $\hat{O} = \hat{O}(\theta,\phi)$ and $\eta = \sqrt{\beta^2-1}$ as

$$\left\langle \hat{O}\right\rangle \approx \frac{\eta}{4\pi\arctan(1/\eta)} \times \int_0^\pi\int_0^{2\pi}\frac{\hat{O}(\theta,\phi)\sin\theta d\phi d\theta}{\left(\sin\theta e^{-i\phi} + i\beta\right)\left(\sin\theta e^{i\phi} - i\beta\right)}. \tag{C18}$$

For example, in the case of $\left\langle \hat{S}_x^2\right\rangle$, we can observe that $\hat{S}_x^2 \to (N/2)^2\sin^2\theta\cos^2\phi$, so in the normal phase we have that

$$\left\langle \hat{S}_x^2\right\rangle \approx \frac{\eta}{4\pi\arctan(1/\eta)} \times \int_0^\pi\int_0^{2\pi}\frac{\left(\frac{N}{2}\right)^2\sin^3\theta\cos^2\phi d\phi d\theta}{\left(\sin\theta e^{-i\phi} + i\beta\right)\left(\sin\theta e^{i\phi} - i\beta\right)} = \left(\frac{N}{2}\right)^2\frac{\eta}{3\beta^2\arctan(1/\eta)}. \tag{C19}$$

In particular for calculating $g_2(0)$, we need to estimate $\left\langle \hat{S}_+\hat{S}_+\hat{S}_-\hat{S}_-\right\rangle$. Given that we are estimating this quantity at the limit of large N, then we expand the operator in the semiclassical approximation at the leading order of N. This implies that $\hat{S}_+\hat{S}_+\hat{S}_-\hat{S}_- = \hat{S}_+^2\hat{S}_-^2 \to \left(N/2\sin\theta e^{i\phi}\right)^2\left(N/2\sin\theta e^{-i\phi}\right)^2 + O\left(N^3\right) \approx (N/2)^4\sin^4\theta$ for large N. In this case, the mathematical expression for

finding $g_2(0)$ at the leading order is given by

$$m_n = \frac{\eta}{4\pi \arctan(1/\eta)} \times \int_0^{\pi}\int_0^{2\pi} \frac{\left(\frac{N}{2}\right)^n \sin^{n+1}\theta d\phi d\theta}{\left(\sin\theta e^{-i\phi}+i\beta\right)\left(\sin\theta e^{i\phi}-i\beta\right)}, \tag{C20}$$

$$g_2(0) \approx \frac{m_4}{m_2^2} \approx \left(\frac{\beta^4}{\eta}\arctan\left(\frac{1}{\eta}\right)-\beta^2-\frac{2}{3}\right) \times \left(\beta^2\arctan\left(\frac{1}{\eta}\right)-\eta\right)^2 \eta\arctan\left(\frac{1}{\eta}\right). \tag{C21}$$

The remanent integrals used to estimate the quantities of interest in Eqs. (13)–(16) are as follows:

$$\left\langle \hat{S}_y \right\rangle \approx \frac{\eta}{4\pi\arctan\left(\frac{1}{\eta}\right)} \times \int_0^{\pi}\int_0^{2\pi} \frac{\frac{N}{2}\sin^2\theta\sin\phi d\phi d\theta}{\left(\sin\theta e^{-i\phi}+i\beta\right)\left(\sin\theta e^{i\phi}-i\beta\right)} = \frac{N}{2}\left(\beta - \frac{\eta}{\beta\arctan(1/\eta)}\right), \tag{C22}$$

$$\left\langle \hat{S}_+\hat{S}_- \right\rangle \approx \left\langle \hat{S}_x^2+\hat{S}_y^2 \right\rangle = \frac{\eta}{4\pi\arctan\left(\frac{1}{\eta}\right)} \times \int_0^{\pi}\int_0^{2\pi} \frac{\left(\frac{N}{2}\right)^2\sin^3\theta d\phi d\theta}{\left(\sin\theta e^{-i\phi}+i\beta\right)\left(\sin\theta e^{i\phi}-i\beta\right)} = \frac{N^2}{4}\left(\beta^2 - \frac{\eta}{\arctan\left(\frac{1}{\eta}\right)}\right). \tag{C23}$$

APPENDIX D: MODIFIED CRF MODEL

The main steady-state features of the dipolar model can be recovered from a much simpler model, which can be solved analytically—the CRF model with one-axis twisting, dephasing, and spontaneous emission. Even though this model has a bistable solution in the superradiant phase. For our chosen initial condition $|g\rangle^{\otimes N}$, we find that the system reaches a steady state very similar to that of the dipolar model. To see this, first we obtain the mean-field steady state, which can be derived from the equations of motion of this model and is given by

$$\begin{aligned}
\langle\dot{\hat{S}}_z\rangle &= -\Omega\langle\hat{S}_y\rangle - \gamma_s\left(\frac{N}{2}+\langle\hat{S}_z\rangle\right) - \Gamma_D(\langle\hat{S}_x\rangle^2+\langle\hat{S}_y\rangle^2),\\
\langle\dot{\hat{S}}_y\rangle &= \Omega\langle\hat{S}_z\rangle + \Gamma_D\langle\hat{S}_z\rangle\langle\hat{S}_y\rangle - \frac{(\gamma_s+4\gamma_d)}{2}\langle\hat{S}_y\rangle + 2\chi\langle\hat{S}_x\rangle\langle\hat{S}_z\rangle,\\
\langle\dot{\hat{S}}_x\rangle &= \Gamma_D\langle\hat{S}_z\rangle\langle\hat{S}_x\rangle - \frac{(\gamma_s+4\gamma_d)}{2}\langle\hat{S}_x\rangle - 2\chi\langle\hat{S}_y\rangle\langle\hat{S}_z\rangle.
\end{aligned} \tag{D1}$$

where, as usual, we have used $\langle\hat{\sigma}_j^{\alpha}\hat{\sigma}_k^{\beta}\rangle = \langle\hat{\sigma}_j^{\alpha}\rangle\langle\hat{\sigma}_k^{\beta}\rangle$ for $j\neq k$ and $\langle\hat{\sigma}_k^{\alpha}\hat{\sigma}_k^{\beta}\rangle = 2i\varepsilon_{\alpha\beta\gamma}\langle\hat{\sigma}_k^{\gamma}\rangle$. For the cooperative emission and one-axis twisting (OAT) terms, we have $\langle\hat{\sigma}_j^{\alpha}\hat{\sigma}_k^{\beta}\rangle = \langle\hat{\sigma}_j^{\alpha}\rangle\langle\hat{\sigma}_k^{\beta}\rangle$ for all j,k [71]. We can see from the above equations that for $\chi=0$, $\langle\dot{\hat{S}}_x\rangle = \Gamma_D\langle\hat{S}_z\rangle\langle\hat{S}_x\rangle - [(\gamma_s+4\gamma_d)/2]\langle\hat{S}_x\rangle \Rightarrow \langle\dot{\hat{S}}_x(t)\rangle = \langle\hat{S}_x(0)\rangle\int dt\exp\{\Gamma_D\langle\hat{S}_z(t)\rangle - [(\gamma_s+4\gamma_d)/2]\}$. Hence, for an initial state with $\langle\hat{S}_x(0)\rangle = 0$ and $\chi=0$, the value of $\langle\hat{S}_x(t)\rangle$ remains zero for the full dynamics of the system. This is because the laser drive is along $\hat{S}_x$, so it commutes with and does not alter $\hat{S}_x$. The other terms are dissipative and they destroy the coherence, $\hat{S}_x$. However, the OAT ($\chi\neq 0$) term causes shearing of the collective Bloch vector about the z axis, which leads to $\hat{S}_x\neq 0$.

For simplicity, from here on, we will use the notation $z\equiv\langle\hat{S}_z\rangle/(N/2)$ and we define new variables (r,ϕ) to express the collective coherence as $\langle\hat{S}_+\rangle/N = re^{i\phi}$, such that $r=\sqrt{\langle\hat{S}_x\rangle^2+\langle\hat{S}_y\rangle^2}/N$ is the contrast and ϕ is the phase in the X-Y plane of the collective Bloch sphere [87]. Then, the MF equations can be expressed in terms of (z,r,ϕ) as

$$\dot{z} = -2\Omega r\sin\phi - \gamma_s(1+z) - 2\Gamma_D N r^2, \tag{D2}$$

$$\dot{r} = \frac{z}{2}(\Omega\sin\phi + \Gamma_D N r) - \frac{(\gamma_s+4\gamma_d)}{2}r, \tag{D3}$$

$$\dot{\phi} = \frac{z}{2r}\Omega\cos\phi + \frac{\chi N z}{2}. \tag{D4}$$

The steady state can be obtained by setting $\dot{z}=\dot{r}=\dot{\phi}=0$. Then, we multiply $4r/z$ to both sides of Eq. (D3) to obtain

$$-2\Omega r\sin\phi - 2\Gamma_D N r^2 = -2(\gamma_s+4\gamma_d)\frac{r^2}{z}. \tag{D5}$$

We plug Eq. (D5) into Eq. (D2) to obtain the steady state as

$$\begin{aligned}
&-2(\gamma_s+4\gamma_d)\frac{r^2}{z} - \gamma_s(1+z) = 0,\\
&\Rightarrow z = -\frac{1}{2} \pm \frac{1}{2}\sqrt{1-8\left(1+\frac{4\gamma_d}{\gamma_s}\right)r^2}.
\end{aligned} \tag{D6}$$

There is a phase transition when the term inside the square root reaches zero and the critical value r_c can be obtained as

$$r_c = \frac{1}{2\sqrt{2(1+4\gamma_d/\gamma_s)}}, \quad z_c = -1/2. \tag{D7}$$

Now, we want to obtain the critical driving strength. We can square and rewrite Eqs. (D2) and (D4) as

$$4\Omega^2 r^2 \sin^2\phi = \left[2\Gamma_D N r^2 + \gamma_s(1+z)^2\right]^2, \tag{D8}$$

$$4\Omega^2 r^2 \cos^2\phi = 4\chi^2 N^2 r^4. \tag{D9}$$

We add Eqs. (D8) and (D9), and keep up to leading-order terms in N to obtain

$$\Omega = \pm\sqrt{(\chi^2+\Gamma_D^2)N^2r^2 + \Gamma_D\gamma_s N(1+z)}. \tag{D10}$$

The sign of Ω determines the direction of the drive along $\pm\hat{S}_x$. For $\chi = 0$, we get back the same MF equations when we flip the signs of Ω and ϕ simultaneously. Thus, the two drive directions $\pm\hat{S}_x$ are physically equivalent. However, a nonzero χ breaks this symmetry. Nevertheless, we get qualitatively similar steady states for the negative and positive values of Ω, so we will only consider the positive value for illustration here. Now, we plug z_c and r_c from Eq. (D7) into Eq. (D10) to obtain the critical drive strength as

$$\Omega_C^{\text{mod-CRF}} = \frac{\Gamma_D}{2\sqrt{2}}\sqrt{\frac{1+(\chi/\gamma_d)^2}{1+(4\gamma_d/\gamma_s)}N^2 + \frac{4\gamma_s}{\Gamma_D}N}. \tag{D11}$$

If we consider the case without dephasing and OAT, i.e., $\gamma_d = 0$ and $\chi = 0$, we recover $\Omega_C \approx \Gamma_D N/(2\sqrt{2})$ [57,71,80]. Thus, the inclusion of spontaneous emission in the CRF model only modifies the critical driving strength by a constant factor, without altering its N scaling. As discussed in the main text, accounting for the frequency shifts from dipolar interactions is important. For that, we set the dephasing rate to be $4\gamma_d/\gamma_s = c_d N$ (c_d=constant). Then, we take the large-N limit, to obtain the critical point as

$$\Omega_C \approx \frac{\Gamma_D}{2\sqrt{2}}\sqrt{N}\sqrt{\frac{1+(\chi/\Gamma_D)^2}{c_d} + \frac{4\gamma_s}{\Gamma_D}}. \tag{D12}$$

In Fig. 16, we show the dynamics of the excitation fraction $n_e(t)$, using the mean-field equations for the modified CRF model [Eq. (D1)], with $c_d = 0.002$. This specific value of c_d is not special and we find qualitatively similar results for other values as long as $c_d \ll 1$. We have taken the continuum limit to obtain $\chi = 1/N\int d^3r \mathrm{Re}\,\tilde{\mathcal{G}}(\vec{r})\rho(\vec{r}) \approx 0.003$ and $\Gamma_D = 1/N\int d^3r \mathrm{Im}\,\tilde{\mathcal{G}}(\vec{r})\rho(\vec{r}) \approx 0.002$, where $\rho(\vec{r})$ [Eq. (A16)] is the pencil-shape distribution of the cloud. Similar to the MF dipolar model, we find that for fixed Ω/γ_s, increasing N leads to larger dephasing and to a suppression of n_e.

1. Modelling random shifts as dephasing

Here, we show how the interaction-induced inhomogeneous shifts lead to a dephasing of the atomic coherences. We describe the interaction-induced dynamical frequency shift at an atom i as $\delta_i(t) = \bar{\Delta}(t) + h_i(t)$, where $\bar{\Delta}(t)$ is the average shift over all the atoms in the cloud and $h_i(t)$ is the position-dependent shift with a zero mean. Considering that $h_i(t)$ is an inhomogeneous frequency shift dominated by local interactions, it varies on a time scale faster than the other time scales of the system. Then, we can write the dynamics of the atomic coherence under $h_i(t)$ as

$$\frac{d}{dt}\langle\hat{\tilde{\sigma}}_i^+(t)\rangle = -ih_i(t)\langle\hat{\tilde{\sigma}}_i^+(t)\rangle + \ldots$$

$$\Rightarrow \langle\hat{\tilde{\sigma}}_i^+(t)\rangle \propto e^{-i\int dt\, h_i(t)}\langle\hat{\tilde{\sigma}}_i^+(0)\rangle,$$

where the slow-time dynamics are included in the proportionality factor. Assuming that the shifts are uncorrelated and random, we can model them as a Gaussian white-noise process, $\overline{h_i(t)h_j(t')} = 4\gamma_d\delta(t-t')\delta_{ij}$, where $4\gamma_d$ is the variance of the shifts. Averaging over this Gaussian process with zero mean and variance $4\gamma_d$, we obtain

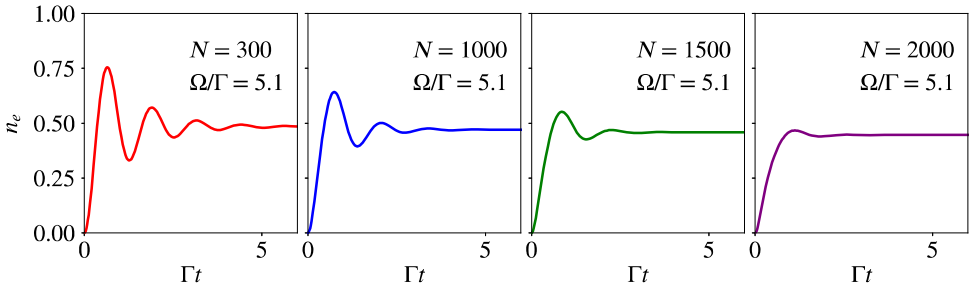

FIG. 16. The dynamics of the excitation fraction n_e for fixed $\Omega/\Gamma \equiv \Omega/\gamma_s = 5.1$ for the CRF model with dephasing ($c_d = 0.002$), OAT, and spontaneous emission.

$\overline{e^{-i\int_0^t dt' h_i(t')}} = e^{-2\gamma_d t}$ [88]. Thus, the random shifts effectively give rise to an overall dephasing of the coherences at a rate $2\gamma_d$.

One key assumption in our model is that these shifts are uncorrelated, which is valid for the densities considered in our paper, where the MF numerics agree well with the beyond-MF methods. Going to large-N systems where near-field interactions dominate, stronger fluctuations will land the system in the beyond-MF regime, in which a more thorough and self-consistent modeling of the correlations is required.

APPENDIX E: CONTRIBUTION OF LASER LIGHT TO THE INTENSITY

We consider a coordinate system in which the center of the atomic cloud is the reference point for the origin, $C = \{0, 0, 0\}$. All the other vectors and positions are defined with respect to this point. Then, the position of an atom j (with respect to C) is given as $\vec{r}_j$. The position of the laser source is $\vec{d}_{\rm L} = \{-d, 0, 0\}$. The position of a point on the detector is $\vec{R} = R\{\cos\theta, \sin\theta\cos\phi, \sin\theta\sin\phi\}$, where θ is the angle from the x axis and ϕ is the azimuthal angle in the y-z plane.

The total electric field and the intensity at a point $\vec{R}$ on the detector are given as

$$\vec{E}^{+}_{\rm total}(\vec{R}) = \vec{E}^{+}_{\rm drive}(\vec{R}) + \langle \vec{E}^{+}_{\rm atoms}(\vec{R})\rangle, \tag{E1}$$

$$I_{\rm total}(\vec{R}) = \vec{E}^{-}_{\rm total}(\vec{R}) \cdot \vec{E}^{+}_{\rm total}(\vec{R}), \tag{E2}$$

where the electric field of the driving laser is

$$\vec{E}^{+}_{\rm drive}(\vec{R}) = E(\vec{R})\hat{e}_{\rm L} = (\hbar\Omega/|\vec{d}|)\hat{e}_{\rm L} e^{i\vec{k}_{\rm L}\cdot\vec{R}'}, \tag{E3}$$

in which $\vec{R}' = \vec{R} - \vec{d}_{\rm L} = (R\cos\theta + d, R\sin\theta\cos\phi, R\sin\theta\sin\phi)$ is the distance vector from the laser source to the detector, the laser polarization is $\hat{e}_{\rm L} = \hat{e}_y$, and its wave vector is $\vec{k}_{\rm L} = (2\pi/\lambda)\hat{x}$ for our system. The electric field of the atomic dipoles is

$$\vec{E}^{+}_{\rm atoms}(\vec{R}) = \frac{\mu_0\omega_0^3}{3\pi\Gamma c}\sum_j \mathbf{G}(\vec{R} - \vec{r}_j)\cdot\hat{e}_{+}|\vec{d}|\hat{\sigma}_j^{-}, \tag{E4}$$

where $\vec{R} - \vec{r}_j$ is the distance vector from atom j to the detector.

Then, considering that the detector is very far from the atomic cloud, it is safe to assume that $R \gg |\vec{r}_j|$ and that the electric field of the atoms is dominated by the far-field limit terms ($R \gg \lambda \Rightarrow \mathbf{G} \propto 1/(k_0 R)$). Under these assumptions, the total intensity (laser + atomic emission) is obtained as

$$I_{\rm total}(\vec{R}) = \left(\frac{\hbar\Gamma}{k_0|\vec{R}||\vec{d}|}\right)^2 \left[\frac{\Omega^2}{\Gamma^2} + \frac{3\Omega}{2\sqrt{2}\Gamma}\sum_j \left(\mathrm{Im}\,\langle\hat{\tilde{\sigma}}_j^{-}\rangle(1 - \sin^2\theta\cos^2\phi) + \mathrm{Re}\,\langle\hat{\tilde{\sigma}}_j^{-}\rangle\frac{\sin(2\theta)}{2}\cos\phi\right) + \frac{9}{16}\sum_{j,k}\frac{(1 + \sin^2\theta\cos^2\phi)}{2}\langle\hat{\sigma}_j^{+}\hat{\sigma}_k^{-}\rangle e^{i\vec{k}\cdot\vec{r}_{jk}}\right], \tag{E5}$$

where $\vec{k} = (2\pi/\lambda)\hat{R}$ and we have defined

$$\begin{aligned}\hat{\tilde{\sigma}}_j^{-} &= \hat{\sigma}_j^{-}\exp(i\vec{k}\cdot(\vec{R} - \vec{r}_j) - i\vec{k}_{\rm L}\cdot\vec{R}')\\ &= \hat{\sigma}_j^{-}\exp(i\vec{k}\cdot(\vec{R} - \vec{r}_j) - i\vec{k}_{\rm L}\cdot(\vec{R} - \vec{d}_{\rm L}))\\ &= \hat{\sigma}_j^{-}\exp(-i(\vec{k}\cdot\vec{r}_j - \vec{k}_{\rm L}\cdot\vec{d}_{\rm L}) - i(\vec{k}_{\rm L} - \vec{k})\cdot\vec{R}).\end{aligned} \tag{E6}$$

The spiral basis has been defined to absorb the laser-induced phase in the Hamiltonian. Keeping the same definition, in the current coordinate system, the spiral basis is defined as $\hat{\tilde{\sigma}}_j^{-} = i\hat{\sigma}_j^{-}e^{-i\vec{k}_{\rm L}\cdot(\vec{r}_j - \vec{d}_{\rm L})}$, where the extra phase factor of i comes from the overlap of the circular polarization of the transition with the laser polarization. So we can rewrite Eq. (E6) in terms of the spiral basis operator as

$$\hat{\tilde{\sigma}}_j^{-} = -i\hat{\tilde{\sigma}}_j^{-}\exp(-i(\vec{k} - \vec{k}_{\rm L})\cdot(\vec{r}_j - \vec{R})) \tag{E7}$$

In the forward direction $\vec{k} = \vec{k}_{\rm L}$, the phases cancel and we have $\hat{\tilde{\sigma}}_j^{-} = -i\hat{\tilde{\sigma}}_j^{-}$. For simplicity, we assume $(\vec{k} - \vec{k}_{\rm L})\cdot\vec{R} \approx 2\pi$, as it is difficult to determine its exact value experimentally. Since we are averaging over $\vec{k}$ to obtain the final numerical values, we expect that changing the value of $|\vec{R}|$ will not change the result significantly.

For simplicity, when including the contribution of the probe light in estimating $\tilde{g}_2(0)$, we have neglected the term

accounting for the interference between the probe and the atomic electric fields.

APPENDIX F: NUMERICAL APPROXIMATIONS

1. Mean-field methods

We use mean-field theory to obtain the dynamics and steady state of the dipolar model. Under mean-field theory, the connected part of the atom-atom correlations is assumed to be negligible. In this case, all correlations can be expressed as products of classical expectation values, as shown in Fig. 17. To benchmark the results obtained from mean-field theory, we use the cumulant method, which goes beyond the mean-field approximation by including two-point connected correlations (for an intuitive picture, see Fig. 17). The MF equations of motion for the dipolar model are given in Appendix B.

2. MACEMF method

We introduce an improved cluster technique that we call MACEMF (moving-average cluster expansion plus mean field). The method combines dynamics considering both local clusters and mean-field interactions with external particles. This method is based on a cluster approximation called MACE [89], developed in the past to deal with dipolar interactions in dilute arrays. It exactly solves for the dynamics inside clusters that are not rigid but instead are adjusted depending of the observable in consideration. For single-point observables $\hat{\sigma}_k$, it chooses a cluster that contains the strongest coupled particles to the k particle in consideration. It disregards the influence of particles outside the cluster. In fact, at a cluster size of 1, MACE essentially reduces to single-particle dynamics.

To account for interaction effects with the particles outside a given cluster, we include them via a mean-field approach. In this way, the dipole-dipole interaction with the outside particles is mapped as an effective time-dependent magnetic field acting upon the atoms in the cluster as shown in Fig. 17. So by combining the exact dynamics within the cluster with the mean-field contributions, we aim to improve the description of the nonequilibrium dynamics of the system.

The clusters are chosen and adapted to optimize the single- or two-particle observables in consideration by including in the cluster the particles that feature the strongest coupling constants to the particle or particles on which the observable is acting.

We generalize it to also include the effect of the external particles to each cluster via the mean-field approximation. This means that the interaction of a given cluster with the surrounding particles is reduced to an effective magnetic field acting on the particles in the cluster. We denote this approach as MACE–mean field (MACEMF). Overall, the method aims to include the best of both the MF and the MACE solutions and improve upon them. In the limit of one particle per cluster, the MACEMF reduces to the MF approximation and if we neglect the MF couplings between clusters, then the MACEMF reduces to the MACE approximation.

For the j particle in the array, the effective Hamiltonian and Lindbladian associated with the cluster of the particle j read as follows:

$$\hat{H}^j_{\mathrm{CMF}} = -\Omega \sum_{i\in C_j} \left(\mathrm{e}^{\mathrm{i}\,\vec{k}_{\mathrm{L}}\cdot\vec{r}_i} \left(e_{\mathrm{L}}\cdot e_0^*\right)\hat{\sigma}_i^+ + \mathrm{h.c.}\right) - \sum_{i,k\in C_j} \mathcal{R}_{ik}\hat{\sigma}_i^+\hat{\sigma}_k^- - \sum_{\substack{i\in C_j,\\ k\notin C_j}} \mathcal{R}_{ik}\left(\hat{\sigma}_i^+\langle\hat{\sigma}_k^-\rangle + \mathrm{h.c.}\right), \tag{F1a}$$

$$L[\hat{\rho}] = \sum_{i,k} \mathcal{I}_{ik}\left(2\hat{\sigma}_k^-\hat{\rho}\hat{\sigma}_i^+ - \{\hat{\sigma}_i^+\hat{\sigma}_k^-,\hat{\rho}\}\right) + \sum_{\substack{i\in C_j,\\ k\notin C_j}} \mathcal{I}_{ik}\left(\langle\hat{\sigma}_k^-\rangle[\hat{\rho}_j,\hat{\sigma}_i^+] - \langle\hat{\sigma}_k^+\rangle[\hat{\rho}_j,\hat{\sigma}_i^-]\right), \tag{F1b}$$

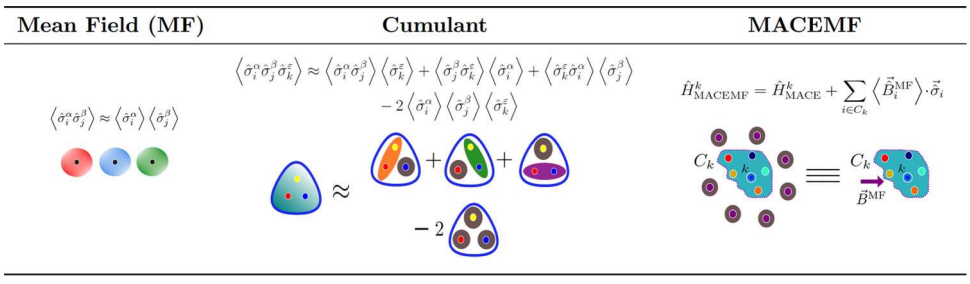

FIG. 17. Numerical approximations. Mean-field (left) uses nonoverlapping clusters, factoring many-body correlations into single-particle values. Cumulant approximation (center), at second order, factors three-body correlations into two-body and single-body correlations. MACEMF (right) treats a cluster and its surrounding particles as a single cluster influenced by an external time-dependent magnetic field.

where C_j denotes the set of particles that are contained in the j-particle cluster and $\hat{\rho}_j$ is the density matrix that describes this cluster.

The cluster C_j is selected by choosing the particles that have the strongest interactions with the j particle (largest $|\mathcal{G}_{jk}|$).

Identifying the second part of the Lindbladian in Eq. (F1a) as an effective element of the Hamiltonian, we can rewrite as follows:

$$\hat{H}^j_{\mathrm{CMF}} = -\sum_{i\in C_j}\left(\left(\Omega e^{i\vec{k}_L\cdot\vec{r}_k}\left(e_L\cdot e_0^*\right)+\sum_{k\notin C_j}\mathcal{R}_{ik}\left\langle\hat{\sigma}_k^-\right\rangle\right)\hat{\sigma}_i^+ + \mathrm{h.c.}\right) - \sum_{i,k\in C_j}\mathcal{R}_{ik}\hat{\sigma}_i^+\hat{\sigma}_k^- - i\sum_{\substack{i\in C_j,\\ k\notin C_j}}\mathcal{I}_{ik}\left(\left\langle\hat{\sigma}_k^-\right\rangle\hat{\sigma}_i^+ - \left\langle\hat{\sigma}_k^+\right\rangle\hat{\sigma}_i^-\right), \tag{F2a}$$

$$L\left[\hat{\rho}\right] = \sum_{i,k\in C_j}\mathcal{I}_{ik}\left(2\hat{\sigma}_k^-\hat{\rho}_j\hat{\sigma}_i^+ - \left\{\hat{\sigma}_i^+\hat{\sigma}_k^-,\hat{\rho}_j\right\}\right). \tag{F2b}$$

Rearranging further the Hamiltonian given in Eq. (F2a), we obtain that

$$\hat{H}^j_{\mathrm{CMF}} = -\sum_{i\in C_j}\left(\left(\Omega e^{i\vec{k}_L\cdot\vec{r}_k}\left(e_L\cdot e_0^*\right)+\sum_{k\notin C_j}\mathcal{G}_{ik}\left\langle\hat{\sigma}_k^-\right\rangle\right)\hat{\sigma}_i^+ + \mathrm{h.c.}\right) - \sum_{i,k\in C_j}\mathcal{R}_{ik}\hat{\sigma}_i^+\hat{\sigma}_k^-. \tag{F3}$$

For estimating second-order correlations of the form $\left\langle\hat{\sigma}_j^\alpha\hat{\sigma}_k^\beta\right\rangle$, where $\alpha,\beta = x,y,z$ and $j\neq k$, we consider the following cases (recall that, by default, $i\in C_i$ for all i):

$$\left\langle\hat{\sigma}_j^\alpha\hat{\sigma}_k^\beta\right\rangle \approx \begin{cases} \dfrac{\left\langle\hat{\sigma}_j^\alpha\hat{\sigma}_k^\beta\right\rangle_{C_j} + \left\langle\hat{\sigma}_j^\alpha\hat{\sigma}_k^\beta\right\rangle_{C_k}}{2}, & \text{if } k\in C_j \text{ and } j\in C_k, \\ \dfrac{\left\langle\hat{\sigma}_j^\alpha\hat{\sigma}_k^\beta\right\rangle_{C_j} + \left\langle\hat{\sigma}_j^\alpha\right\rangle\left\langle\hat{\sigma}_k^\beta\right\rangle}{2}, & \text{if } k\in C_j \text{ and } j\notin C_k, \\ \dfrac{\left\langle\hat{\sigma}_j^\alpha\right\rangle\left\langle\hat{\sigma}_k^\beta\right\rangle + \left\langle\hat{\sigma}_j^\alpha\hat{\sigma}_k^\beta\right\rangle_{C_k}}{2}, & \text{if } k\notin C_j \text{ and } j\in C_k, \\ \left\langle\hat{\sigma}_j^\alpha\right\rangle\left\langle\hat{\sigma}_k^\beta\right\rangle, & \text{if } k\notin C_j \text{ and } j\notin C_k. \end{cases} \tag{F4}$$

Here, $\left\langle\hat{\mathcal{O}}\right\rangle_{C_j} = \mathrm{Tr}(\hat{\rho}_j\hat{\mathcal{O}})$, which represents the expected value of the operator $\hat{\mathcal{O}}$ with respect to the cluster C_j. Similar decompositions can be used to estimate higher-order correlations.

APPENDIX G: VALIDITY OF MEAN-FIELD THEORY

In this appendix, we benchmark the steady-state properties of the MF dipolar model by comparing with the results

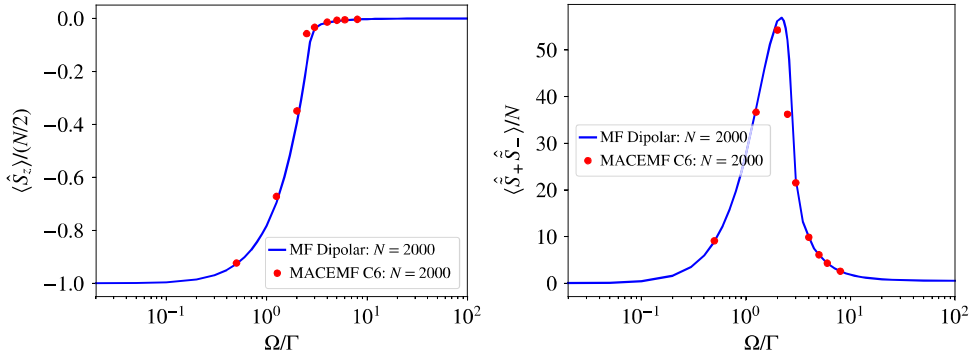

FIG. 18. Comparing MACEMF C6, i.e., a cluster size of six atoms, with MF in the steady state for $N = 2000$.

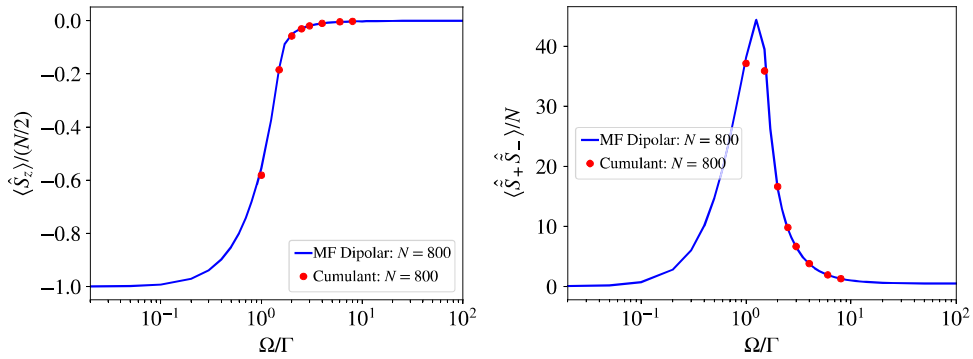

FIG. 19. Comparing cumulant (single realization) with MF (averaged over ten realizations) in the steady state for $N = 800$.

of beyond-MF methods such as MACEMF, exact diagonalization (ED), and cumulant approximation. We average the data over approximately ten realizations for the MF, MACEMF, and ED results.

MACEMF includes short-range beyond-MF correlations by treating them exactly (using ED) within a given cluster size. In Fig. 18, we show that the MF steady-state atomic inversion and forward intensity for $N = 2000$ agree extremely well with those obtained from MACEMF with cluster size 6, across a range of Ω/Γ spanning the different dynamical phases. We find that the MACEMF results do not change appreciably as we increase the cluster size beyond 6. The agreement between MF and MACEMF suggests that the effect of short-range interactions is minimal in the steady state and gets washed out at these densities. At higher densities, the inter-atomic distances would be shorter and $1/r^3$ interactions would dominate, causing MF to break down.

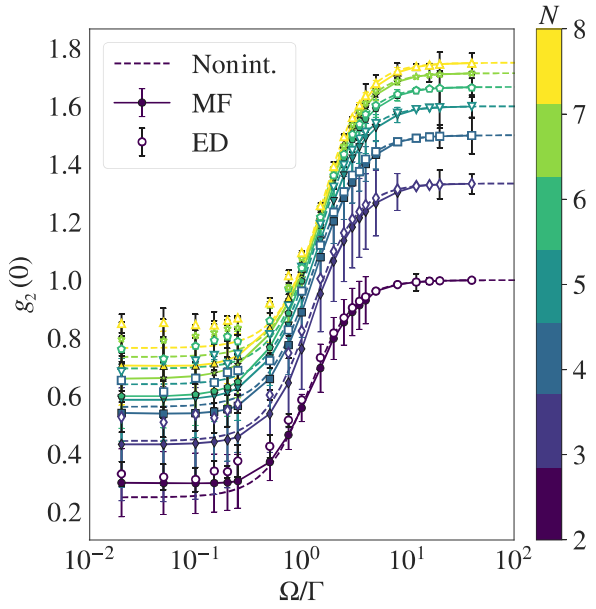

FIG. 20. Comparing ED with MF for the two-photon correlation function in the steady state $\tilde{g}_2(0)$.

The cumulant method includes long-range beyond-MF two-point correlations. In Fig. 19, we show that the MF steady-state atomic inversion and forward intensity for $N = 800$ agree extremely well with those obtained from the cumulant method, across a range of Ω/Γ in the intermediate-driving regime, where we expect the effect of correlations to be most apparent, compared to the weak and strong-driving regimes. From the excellent agreement between MF and cumulant, we can see that the effect of long-range correlations is negligible in the steady state of our system. Cumulant numerics with higher densities and larger N take extremely long run times, restricting us up to $N = 800$ here. However, as we already see good agreement with MACEMF at $N = 2000$, we do not expect the cumulant results to change at least qualitatively up to $N = 2000$.

In Fig. 20, we compare the two-photon correlation function $\tilde{g}_2(0)$ in the steady state of the MF dipolar model with that obtained from ED. We choose small N for this comparison, as the Hilbert space grows exponentially with N and ED becomes numerically intractable for larger N. We keep the OD fixed while reducing N, so that the interaction strength is still similar to that of the $N = 2000$ system. We find that at small Ω/Γ, there is a lot of variance in $\tilde{g}_2(0)$ across realizations and within these error bars, there seems to be a fair agreement between ED and MF. At large Ω/Γ, the system becomes single-particle-like and the error bars get smaller as interactions do not play a role and the change in atomic positions across realizations stops affecting the physics. Hence, there is a much better agreement between ED and MF in this regime. Due to finite N corrections, $\tilde{g}_2(0)$ does not go from exactly 1 to 2, as the drive strength is increased.

[1] M. Gross and S. Haroche, Superradiance: An essay on the theory of collective spontaneous emission, Phys. Rep. **93,** 301 (1982).

[2] K. Hammerer, A. S. Sørensen, and E. S. Polzik, Quantum interface between light and atomic ensembles, Rev. Mod. Phys. **82,** 1041 (2010).

[3] M. J. Stephen, First-order dispersion forces, J. Chem. Phys. **40**, 669 (1964).

[4] R. H. Lehmberg, Radiation from an N-atom system. I. General formalism, Phys. Rev. A **2**, 883 (1970).

[5] R. Friedberg, S. Hartmann, and J. Manassah, Frequency shifts in emission and absorption by resonant systems of two-level atoms, Phys. Rep. **7**, 101 (1973).

[6] D. F. V. James, Frequency shifts in spontaneous emission from two interacting atoms, Phys. Rev. A **47**, 1336 (1993).

[7] S. D. Jenkins and J. Ruostekoski, Controlled manipulation of light by cooperative response of atoms in an optical lattice, Phys. Rev. A **86**, 031602(R) (2012).

[8] J. Javanainen and J. Ruostekoski, Light propagation beyond the mean-field theory of standard optics, Opt. Express **24**, 993 (2016).

[9] D. Porras and J. I. Cirac, Collective generation of quantum states of light by entangled atoms, Phys. Rev. A **78**, 053816 (2008).

[10] A. A. Svidzinsky, J.-T. Chang, and M. O. Scully, Dynamical evolution of correlated spontaneous emission of a single photon from a uniformly excited cloud of N atoms, Phys. Rev. Lett. **100**, 160504 (2008).

[11] T. Ido, T. H. Loftus, M. M. Boyd, A. D. Ludlow, K. W. Holman, and J. Ye, Precision spectroscopy and density-dependent frequency shifts in ultracold Sr, Phys. Rev. Lett. **94**, 153001 (2005).

[12] M. O. Scully, Collective Lamb shift in single photon Dicke superradiance, Phys. Rev. Lett. **102**, 143601 (2009).

[13] R. Röhlsberger, K. Schlage, B. Sahoo, S. Couet, and R. Rüffer, Collective lamb shift in single-photon superradiance, Science **328**, 1248 (2010).

[14] J. Keaveney, A. Sargsyan, U. Krohn, I. G. Hughes, D. Sarkisyan, and C. S. Adams, Cooperative Lamb shift in an atomic vapor layer of nanometer thickness, Phys. Rev. Lett. **108**, 173601 (2012).

[15] Z. Meir, O. Schwartz, E. Shahmoon, D. Oron, and R. Ozeri, Cooperative Lamb shift in a mesoscopic atomic array, Phys. Rev. Lett. **113**, 193002 (2014).

[16] J. Javanainen, J. Ruostekoski, Y. Li, and S.-M. Yoo, Shifts of a resonance line in a dense atomic sample, Phys. Rev. Lett. **112**, 113603 (2014).

[17] S. L. Bromley, B. Zhu, M. Bishof, X. Zhang, T. Bothwell, J. Schachenmayer, T. L. Nicholson, R. Kaiser, S. F. Yelin, M. D. Lukin, *et al.*, Collective atomic scattering and motional effects in a dense coherent medium, Nat. Commun. **7**, 11039 (2016).

[18] S. J. Roof, K. J. Kemp, M. D. Havey, and I. M. Sokolov, Observation of single-photon superradiance and the cooperative Lamb shift in an extended sample of cold atoms, Phys. Rev. Lett. **117**, 073003 (2016).

[19] J. Rui, D. Wei, A. Rubio-Abadal, S. Hollerith, J. Zeiher, D. M. Stamper-Kurn, C. Gross, and I. Bloch, A subradiant optical mirror formed by a single structured atomic layer, Nature **583**, 369 (2020).

[20] H. Ma and S. F. Yelin, Collective Lamb shift and modified linewidth of an interacting atomic gas, ArXiv:2305.01865.

[21] N. O. Gjonbalaj, S. Ostermann, and S. F. Yelin, Modifying cooperative decay via disorder in atom arrays, Phys. Rev. A **109**, 013720 (2024).

[22] S. Jennewein, L. Brossard, Y. R. P. Sortais, A. Browaeys, P. Cheinet, J. Robert, and P. Pillet, Coherent scattering of near-resonant light by a dense, microscopic cloud of cold two-level atoms: Experiment versus theory, Phys. Rev. A **97**, 053816 (2018).

[23] A. Glicenstein, G. Ferioli, N. Šibalić, L. Brossard, I. Ferrier-Barbut, and A. Browaeys, Collective shift in resonant light scattering by a one-dimensional atomic chain, Phys. Rev. Lett. **124**, 253602 (2020).

[24] M. O. Scully, E. S. Fry, C. H. R. Ooi, and K. Wódkiewicz, Directed spontaneous emission from an extended ensemble of N atoms: Timing is everything, Phys. Rev. Lett. **96**, 010501 (2006).

[25] M. O. Scully, Correlated spontaneous emission on the Volga, Laser Phys. **17**, 635 (2007).

[26] P. R. Berman, Energy conservation in collective coherent emission by dipole oscillators, Am. J. Phys. **78**, 1323 (2010).

[27] R. A. de Oliveira, M. S. Mendes, W. S. Martins, P. L. Saldanha, J. W. R. Tabosa, and D. Felinto, Single-photon superradiance in cold atoms, Phys. Rev. A **90**, 023848 (2014).

[28] M. O. Araújo, I. Krešić, R. Kaiser, and W. Guerin, Superradiance in a large and dilute cloud of cold atoms in the linear-optics regime, Phys. Rev. Lett. **117**, 073002 (2016).

[29] R. T. Sutherland and F. Robicheaux, Coherent forward broadening in cold atom clouds, Phys. Rev. A **93**, 023407 (2016).

[30] B. Zhu, J. Cooper, J. Ye, and A. M. Rey, Light scattering from dense cold atomic media, Phys. Rev. A **94**, 023612 (2016).

[31] W. Guerin, in *Advances in Atomic, Molecular, and Optical Physics*, edited by L. F. DiMauro, H. Perrin, and S. F. Yelin (Academic Press, 2023), Vol. 72, p. 253.

[32] J. Pellegrino, R. Bourgain, S. Jennewein, Y. R. P. Sortais, A. Browaeys, S. D. Jenkins, and J. Ruostekoski, Observation of suppression of light scattering induced by dipole-dipole interactions in a cold-atom ensemble, Phys. Rev. Lett. **113**, 133602 (2014).

[33] S. Jennewein, M. Besbes, N. J. Schilder, S. D. Jenkins, C. Sauvan, J. Ruostekoski, J.-J. Greffet, Y. R. P. Sortais, and A. Browaeys, Coherent scattering of near-resonant light by a dense microscopic cold atomic cloud, Phys. Rev. Lett. **116**, 233601 (2016).

[34] D. Pavolini, A. Crubellier, P. Pillet, L. Cabaret, and S. Liberman, Experimental evidence for subradiance, Phys. Rev. Lett. **54**, 1917 (1985).

[35] T. Bienaimé, N. Piovella, and R. Kaiser, Controlled dicke subradiance from a large cloud of two-level systems, Phys. Rev. Lett. **108**, 123602 (2012).

[36] T. Bienaimé, R. Bachelard, N. Piovella, and R. Kaiser, Cooperativity in light scattering by cold atoms, Fortschr. Phys. **61**, 377 (2013).

[37] M. O. Scully, Single photon subradiance: Quantum control of spontaneous emission and ultrafast readout, Phys. Rev. Lett. **115**, 243602 (2015).

[38] W. Guerin, M. O. Araújo, and R. Kaiser, Subradiance in a large cloud of cold atoms, Phys. Rev. Lett. **116**, 083601 (2016).

[39] O. Rubies-Bigorda, S. Ostermann, and S. F. Yelin, Dynamic population of multiexcitation subradiant states in incoherently excited atomic arrays, Phys. Rev. A **107**, L051701 (2023).
[40] G. Ferioli, A. Glicenstein, L. Henriet, I. Ferrier-Barbut, and A. Browaeys, Storage and release of subradiant excitations in a dense atomic cloud, Phys. Rev. X **11**, 021031 (2021).
[41] M.-T. Rouabah, M. Samoylova, R. Bachelard, P. W. Courteille, R. Kaiser, and N. Piovella, Coherence effects in scattering order expansion of light by atomic clouds, J. Opt. Soc. Am. A **31**, 1031 (2014).
[42] D. Plankensteiner, L. Ostermann, H. Ritsch, and C. Genes, Selective protected state preparation of coupled dissipative quantum emitters, Sci. Rep. **5**, 16231 (2015).
[43] R. J. Bettles, S. A. Gardiner, and C. S. Adams, Cooperative eigenmodes and scattering in one-dimensional atomic arrays, Phys. Rev. A **94**, 043844 (2016).
[44] G. Facchinetti, S. D. Jenkins, and J. Ruostekoski, Storing light with subradiant correlations in arrays of atoms, Phys. Rev. Lett. **117**, 243601 (2016).
[45] R. T. Sutherland and F. Robicheaux, Collective dipole-dipole interactions in an atomic array, Phys. Rev. A **94**, 013847 (2016).
[46] H. H. Jen, M.-S. Chang, and Y.-C. Chen, Cooperative single-photon subradiant states, Phys. Rev. A **94**, 013803 (2016).
[47] C. D. Mink and M. Fleischhauer, Collective radiative interactions in the discrete truncated Wigner approximation, SciPost Phys. **15**, 233 (2023).
[48] S. J. Masson and A. Asenjo-Garcia, Universality of Dicke superradiance in arrays of quantum emitters, Nat. Commun. **13**, 2285 (2022).
[49] O. Rubies-Bigorda, S. Ostermann, and S. F. Yelin, Characterizing superradiant dynamics in atomic arrays via a cumulant expansion approach, Phys. Rev. Res. **5**, 013091 (2023).
[50] S. J. Masson, J. P. Covey, S. Will, and A. Asenjo-Garcia, Dicke superradiance in ordered arrays of multilevel atoms, PRX Quantum **5**, 010344 (2024).
[51] F. Robicheaux and D. A. Suresh, Intensity effects of light coupling to one- or two-atom arrays of infinite extent, Phys. Rev. A **108**, 013711 (2023).
[52] J. Ruostekoski, Cooperative quantum-optical planar arrays of atoms, Phys. Rev. A **108**, 030101 (2023).
[53] S. Ostermann, O. Rubies-Bigorda, V. Zhang, and S. F. Yelin, Breakdown of steady-state superradiance in extended driven atomic arrays, Phys. Rev. Research **6**, 023206.
[54] J. Ruostekoski, Superradiant phase transition in a large interacting driven atomic ensemble in free space, ArXiv:2404.12939.
[55] R. H. Dicke, Coherence in spontaneous radiation processes, Phys. Rev. **93**, 99 (1954).
[56] H. J. Carmichael and D. F. Walls, Hysteresis in the spectrum for cooperative resonance fluorescence, J. Phys. B: At. Mol. Phys. **10**, L685 (1977).
[57] D. F. Walls, P. D. Drummond, S. S. Hassan, and H. J. Carmichael, Non-equilibrium phase transitions in cooperative atomic systems, Prog. Theor. Phys. Suppl. **64**, 307 (1978).
[58] P. Drummond and H. Carmichael, Volterra cycles and the cooperative fluorescence critical point, Opt. Commun. **27**, 160 (1978).
[59] D. F. Walls, Cooperative fluorescence from N coherently driven two-level atoms, J. Phys. B: At. Mol. Phys. **13**, 2001 (1980).
[60] L. M. Narducci, D. H. Feng, R. Gilmore, and G. S. Agarwal, Transient and steady-state behavior of collective atomic systems driven by a classical field, Phys. Rev. A **18**, 1571 (1978).
[61] G. Ferioli, A. Glicenstein, I. Ferrier-Barbut, and A. Browaeys, A non-equilibrium superradiant phase transition in free space, Nat. Phys. **19**, 1345 (2023).
[62] B. R. Mollow, Power spectrum of light scattered by two-level systems, Phys. Rev. **188**, 1969 (1969).
[63] R. Loudon, *The Quantum Theory of Light* (Oxford University Press, Oxford, 2000).
[64] F. H. Bonifacio and P. Schwendimann, Quantum statistical theory of superradiance. I, Phys. Rev. A **4**, 302 (1971).
[65] K. Hepp and E. H. Lieb, On the superradiant phase transition for molecules in a quantized radiation field: The Dicke maser model, Ann. Phys. (NY) **76**, 360 (1973).
[66] Y. K. Wang and F. T. Hioe, Phase transition in the Dicke model of superradiance, Phys. Rev. A **7**, 831 (1973).
[67] M. M. Roses and E. G. Dalla Torre, Dicke model, PLoS ONE **15**, 1 (2020).
[68] A. González-Tudela and D. Porras, Mesoscopic entanglement induced by spontaneous emission in solid-state quantum optics, Phys. Rev. Lett. **110**, 080502 (2013).
[69] J. Hannukainen and J. Larson, Dissipation-driven quantum phase transitions and symmetry breaking, Phys. Rev. A **98**, 042113 (2018).
[70] O. Somech, Y. Shimshi, and E. Shahmoon, Heisenberg-Langevin approach to driven superradiance, Phys. Rev. A **108**, 023725 (2023).
[71] H. J. Carmichael, Analytical and numerical results for the steady state in cooperative resonance fluorescence, J. Phys. B: At. Mol. Phys. **13**, 3551 (1980).
[72] V. Link, K. Luoma, and W. T. Strunz, Revealing the nature of non-equilibrium phase transitions with quantum trajectories, Phys. Rev. A **99**, 062120 (2019).
[73] W. L. Barnes, S. A. R. Horsley, and W. L. Vos, Classical antennas, quantum emitters, and densities of optical states, J. Opt. **22**, 073501 (2020).
[74] A. S. Kuraptsev, I. M. Sokolov, and M. D. Havey, Angular distribution of single-photon superradiance in a dilute and cold atomic ensemble, Phys. Rev. A **96**, 023830 (2017).
[75] D. E. Chang, J. Ye, and M. D. Lukin, Controlling dipole-dipole frequency shifts in a lattice-based optical atomic clock, Phys. Rev. A **69**, 023810 (2004).
[76] R. B. Hutson, W. R. Milner, L. Yan, J. Ye, and C. Sanner, Observation of millihertz-level cooperative Lamb shifts in an optical atomic clock, Science **383**, 384 (2024).
[77] O. Morice, Y. Castin, and J. Dalibard, Refractive index of a dilute Bose gas, Phys. Rev. A **51**, 3896 (1995).
[78] L. Chomaz, L. Corman, T. Yefsah, R. Desbuquois, and J. Dalibard, Absorption imaging of a quasi-two-dimensional gas: A multiple scattering analysis, New J. Phys. **14**, 055001 (2012).

[79] A. M. Rey, L. Jiang, and M. D. Lukin, Quantum-limited measurements of atomic scattering properties, Phys. Rev. A **76**, 053617 (2007).

[80] D. Roberts and A. A. Clerk, Exact solution of the infinite-range dissipative transverse-field Ising model, Phys. Rev. Lett. **131**, 190403 (2023).

[81] C. Qu and A. M. Rey, Spin squeezing and many-body dipolar dynamics in optical lattice clocks, Phys. Rev. A **100**, 041602 (2019).

[82] D. Goncalves, L. Bombieri, G. Ferioli, S. Pancaldi, I. Ferrier-Barbut, A. Browaeys, E. Shamoon, and D. E. Chang, Driven-dissipative phase separation in free-space atomic ensembles, arXiv:2403.15237.

[83] G. Ferioli, S. Pancaldi, I. Ferrier-Barbut, and A. Browaeys, Private communication.

[84] A. Asenjo-Garcia, H. J. Kimble, and D. E. Chang, Optical waveguiding by atomic entanglement in multilevel atom arrays, Proc. Natl. Acad. Sci. **116**, 25503 (2019).

[85] T. Bilitewski, A. P. N. Orioli, C. Sanner, L. Sonderhouse, R. B. Hutson, L. Yan, W. R. Milner, J. Ye, and A. M. Rey, Disentangling Pauli blocking of atomic decay from cooperative radiation and atomic motion in a 2D Fermi gas, Phys. Rev. Lett. **128**, 093001 (2022).

[86] D. Barberena, R. J. Lewis-Swan, J. K. Thompson, and A. M. Rey, Driven-dissipative quantum dynamics in ultralong-lived dipoles in an optical cavity, Phys. Rev. A **99**, 053411 (2019).

[87] K. Tucker, D. Barberena, R. J. Lewis-Swan, J. K. Thompson, J. G. Restrepo, and A. M. Rey, Facilitating spin squeezing generated by collective dynamics with single-particle decoherence, Phys. Rev. A **102**, 051701(R) (2020).

[88] K. E. Dorfman, P. Wei, J. Liu, and R. Li, Quantum interference and collisional dynamics in excited bounds states revealed by time-resolved pump-high-harmonic-generation-probe spectroscopy, Opt. Express **27**, 7147 (2019).

[89] K. R. A. Hazzard, B. Gadway, M. Foss-Feig, B. Yan, S. A. Moses, J. P. Covey, N. Y. Yao, M. D. Lukin, J. Ye, D. S. Jin, *et al.*, Many-body dynamics of dipolar molecules in an optical lattice, Phys. Rev. Lett. **113**, 195302 (2014).